Kent Academic Repository

Full text document (pdf)

Citation for published version

Wang, Lijuan and Liu, Jinyu and Yan, Yong and Wang, Xue and Wang, Tao (2016) Gas-liquid Two-phase Flow Measurement Using Coriolis Flowmeters Incorporating Artificial Neural Network, Support Vector Machine and Genetic Programming Algorithms. IEEE Transactions on Instrumentation and Measurement . ISSN 0018-9456. (In press)

DOI

http://doi.org/10.1109/TIM.2016.2634630

Link to record in KAR

http://kar.kent.ac.uk/58588/

Document Version

Author's Accepted Manuscript

Copyright & reuse
Content in the Kent Academic Repository is made available for research purposes. Unless otherwise stated all content is protected by copyright and in the absence of an open licence (eg Creative Commons), permissions for further reuse of content should be sought from the publisher, author or other copyright holder.

Versions of research
The version in the Kent Academic Repository may differ from the final published version.
Users are advised to check **http://kar.kent.ac.uk** for the status of the paper. **Users should always cite the published version of record.**

Enquiries
For any further enquiries regarding the licence status of this document, please contact:
researchsupport@kent.ac.uk

If you believe this document infringes copyright then please contact the KAR admin team with the take-down information provided at **http://kar.kent.ac.uk/contact.html**

KAR Kent Academic Repository

University of Kent

IM-16-12529R1

Title: Gas-liquid Two-phase Flow Measurement Using Coriolis Flowmeters Incorporating Artificial Neural Network, Support Vector Machine and Genetic Programming Algorithms

Authors: Lijuan Wang [a]

Jinyu Liu [a]

Yong Yan [a] (Corresponding author)

Xue Wang [b]

Tao Wang [c]

Addresses: [a] School of Engineering and Digital Arts

University of Kent, Canterbury, Kent CT2 7NT, U.K.

Tel: 00441227823015

Fax: 00441227456084

Email: y.yan@kent.ac.uk

[b] School of Mathematics, Statistics and Actuarial Science

University of Kent

Canterbury

Kent CT2 7NF, U.K.

[c] KROHNE Ltd.

34-38 Rutherford Drive

Wellingborough

NN8 6AE, U.K.

ABSTRACT

Coriolis flowmeters are well established for the mass flow measurement of single phase flow with high accuracy. In recent years attempts have been made to apply Coriolis flowmeters to measure two-phase flow. This paper presents data driven models that are incorporated in Coriolis flowmeters to measure both the liquid mass flowrate and the gas volume fraction of a two-phase flow mixture. Experimental work was conducted on a purpose-built two-phase flow test rig on both horizontal and vertical pipelines for a liquid mass flowrate ranging from 700 kg/h to 14500 kg/h and a gas volume fraction between 0 and 30%. Artificial Neural Network (ANN), Support Vector Machine (SVM) and Genetic Programming (GP) models are established through training with experimental data. The performance of BP-ANN (Back Propagation - ANN), RBF-ANN (Radial Basis Function - ANN), SVM and GP models is assessed and compared. Experimental results suggest that the SVM models are superior to the BP-ANN, RBF-ANN and GP models for two-phase flow measurement in terms of robustness and accuracy. For liquid mass flowrate measurement with the SVM models, 93.49% of the experimental data yield a relative error less than ±1% on the horizontal pipeline whilst 96.17% of the results are within ±1% on the vertical installation. The SVM models predict gas volume fraction with a relative error less than ±10% for 93.10% and 94.25% of the test conditions on horizontal and vertical installations, respectively.

Index Terms–Two-phase flow, flow measurement, Coriolis mass flowmeter, gas volume fraction, artificial neural network, support vector machine, genetic programming.

I. INTRODUCTION

Gas-liquid two-phase flow is widely seen in oil and gas fields, chemical engineering, food processing and other industrial processes. The accurate measurement of the flowrate of a two-phase mixture is challenging in industry. Significant research based on traditional flowmeters for two-phase flow measurement has been conducted, such as Venturi, V-cone, turbine, vortex and slotted orifice meters [1-3]. The determination of gas volume fraction of two-phase flow is crucial for the optimization of some industrial processes. Resistive sensors, capacitive sensors, electrical capacitance tomography, electrical resistance tomography and microwave probes have been proposed for the phase fraction measurement of two-phase flow [4-6]. These techniques are often referred to as direct method since the systems are designed to measure the desired two-phase flow characteristics directly. Due to the difficult nature of two-phase flow and complexity of the sensing systems, applications of such direct two-phase flowmeters have achieved limited success in industry.

Indirect techniques based on traditional sensors incorporating soft-computing algorithms such as artificial neural network (ANN), support vector machine (SVM), least-squares SVM and extreme learning machine together with genetic algorithms or particle swarm optimization etc., have also been applied to two-phase or multi-phase flow measurement or flow regime identification [7-10]. Coriolis flowmeters, as one of the most accurate single-phase mass flowmeters, have been successfully applied to a range of industrial applications. In recent years, many researchers have attempted to use Coriolis flowmeters for two-phase or multiphase flow measurement [11]. However, despite recent progress in sensor and transmitter technologies, improving the accuracy for mass flow metering of liquid with entrained gas still remains a challenge. A bubble effect model was proposed to study gas-liquid two-phase flow for Coriolis flowmeters [12], but it

cannot deal with positive errors in the mass flow measurement. Subsequently, Liu et al [13] used a neural network to correct mass flow errors in a Coriolis mass flowmeter which was based on a horizontal flow tube and the flow rate was limited to 1.5~3.6 kg/s. The multi-layer perceptron and radial basis function networks include four inputs, including temperature, damping, density drop and flowrate to estimate mass flow errors. Although most of the mass flow errors were reduced to within ±2%, the gas entrainment was not quantified and different installation conditions were not considered. A method based on fuzzy inference was proposed to correct the mass flow errors of a Coriolis flowmeter for the measurement of two-phase flow [14]. The fuzzy system accepts damping, drop in density and apparent mass flowrate as inputs to generate corrected mass flowrate. Lari et al [15] applied a neuro-fuzzy algorithm to the error correction of a Coriolis mass flowmeter for air-water two-phase flow measurement. However, the experimental data and results were not explained in detail in [14] and [15]. Hou et al [16] developed a digital Coriolis flow transmitter and tested a commercial Coriolis flowmeter. The measurement errors achieved under gas-liquid two-phase flow conditions were corrected using a feed-forward neural network with two inputs - apparent liquid mass flowrate and apparent drop in density. Xing et al [17] applied a Coriolis flowmeter in combination with an ultrasonic flowmeter to measure the individual mass flowrates of gas-liquid two-phase flow under low liquid loading. The root-mean-square errors of gas and liquid mass flowrates were 3.09% and 12.78%, respectively. Ma et al [18] used a 25 mm bore Coriolis flowmeter together with SVM algorithms to measure the overall mass flowrate of oil-water two-phase flow and achieved relative errors within ±1%. The mass flowrate of individual phase was obtained with the maximum error of ±8%. However, it is known that the gas entrained in a liquid flow affects significantly the performance of Coriolis flowmeters, especially

under different flow regimes [11]. Moreover, very little research has been undertaken to date to predict the gas volume fraction from the outputs of a Coriolis flowmeter.

Owning to the good reproducibility of the measurement errors of Coriolis flowmeters under two-phase flow conditions, data driven models such as ANN, SVM and Genetic Programming (GP) have the potential to correct the liquid mass flowrate and predict gas volume fraction. In the present study, experimental work was undertaken on a purpose-built one-inch (25 mm) bore air-water two-phase flow test rig. Coriolis flowmeters (KROHNE OPTIMASS 6400 S25) in conjunction with DP transducers were applied to obtain liquid mass flowrate and gas volume fraction on both horizontal and vertical pipes. Parametric dependency along with input variable selection for the data driven models are investigated based on the Partial Mutual Information (PMI) algorithm [19, 20]. Four data driven models based on Back Propagation-ANN (BP-ANN), Radial Basis Function-ANN (RBF-ANN), SVM and GP, respectively, are established and validated through training and testing with experimental data. The performances of the four models are evaluated and compared in terms of robustness and accuracy. The basic principle of BP-ANN modelling with some preliminary results was reported at the 2016 IEEE International Instrumentation and Measurement Technology Conference [21]. This paper presents in detail the principles, structures, training and performance comparisons of the BP-ANN, RBF-ANN, SVM and GP models.

II. METHODOLOGY

A. Overall measurement strategy

ANN, SVM and GP are common data driven models for modelling a nonlinear system with multiple inputs and outputs [22-26]. These techniques learn from history data and given examples

by constructing an input-output mapping in order to perform estimations of desired outputs. Fig. 1 shows the principle and structure of the measurement system. The data driven models accept variables from a Coriolis flowmeter and a DP transducer while the output gives the corrected mass flowrate or predicted gas volume fraction. The analysis of parametric dependence and input variable selection for the data driven models based on the experimental data is presented in Section III. C. Since the volume of data is often limited in practice, it is appropriate to design a separate model for each desired output. The structure of each data driven model based on ANN, SVM and GP will be explained in detail in the following sections.

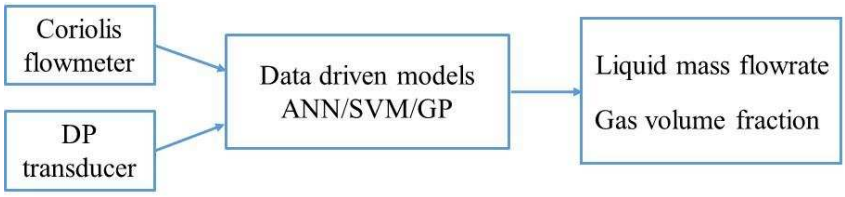

Fig. 1. Principle and structure of the measurement system.

B. BP-ANN

BP-ANN is a multilayer feed-forward neural network trained with a back-propagation learning algorithm, which is one of the most common neural networks. A BP-ANN consists of an input layer, one or more hidden layers and an output layer. The hidden layer connects the input and output layers and represents their quantitative relationship. In general, a neural network with a single-hidden layer of sufficient neurons is able to represent any nonlinear problem. In consideration of the simplicity of the ANN structure, a single-hidden layer is chosen and investigated in this study.

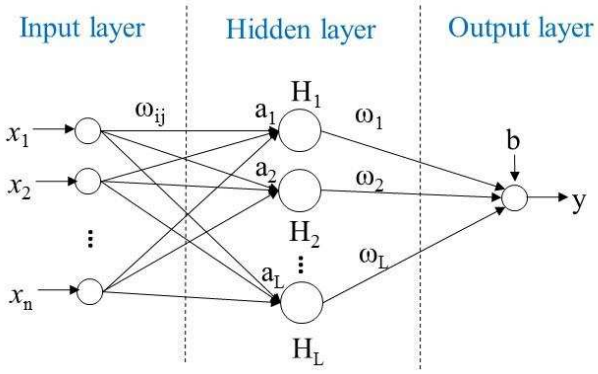

Fig. 2. Structure of a BP-ANN.

As shown in Fig. 2, $x=[x_1,x_2, \ldots, x_n]^T$ is an input sample and y is the desired output. Assume y is the linear output of the hidden neurons and a transfer function f(x) is used on the neurons, the ANN is modelled as:

$$y_{BP} = \sum_{j=1}^{L} \omega_j H_j + b = \sum_{j=1}^{L} \omega_j f\left(\sum_{i=1}^{n} \omega_{ij} x_i + a_j\right) + b \tag{1}$$

where n and L are the numbers of input variables and hidden nodes. ω_j is the weight connecting the j^{th} hidden node and the output node, ω_{ij} is the weight connecting the i^{th} input node to the j^{th} hidden node. a_j and b are the biases on the j^{th} hidden node and the output node. In this study, the hyperbolic tangent sigmoid function is used as a transfer function on hidden neurons and presented by

$$f(x) = \frac{2}{1+e^{-2x}} - 1 \tag{2}$$

The learning algorithm is described as a procedure that consists of adjusting the weights and biases of a network, to minimize an error function between the network output and desired output for a given set of inputs. The BP algorithm has been widely applied to solving practical problems. However, the BP algorithm has the disadvantage of slow convergence and long training time.

Additionally, the success of the BP algorithm depends on the user-dependent parameters, such as initialization and structure of the ANN.

C. RBF-ANN

RBF-ANN has a fixed three layer structure (Fig. 3) and uses a type of radial basis function as an activation function to the hidden nodes. The output of the network is a linear combination of radial basis functions of the inputs and neuron parameters. The radial basis function measures the distance between the input vectors and weight vectors and is typically taken to be the Gaussian function. Thus the output of the network is given by

$$y_{RBF} = \sum_{j=1}^{L} \omega_j H_j = \sum_{j=1}^{L} \omega_j \exp\left(-\frac{1}{2\sigma^2}\left\|x - C_j\right\|^2\right) \quad (3)$$

where C_j is the centre vector for the j^{th} hidden node and determined by the K-means clustering method. $\|x - C_j\|$ is the Euclidean norm and σ^2 is the variance of the Gaussian function.

An RBF network with enough hidden nodes can approximate any continuous function with arbitrary precision. Moreover, as a local approximation network, the RBF neural network has the advantages of simple structure, less adjective parameters and fast training.

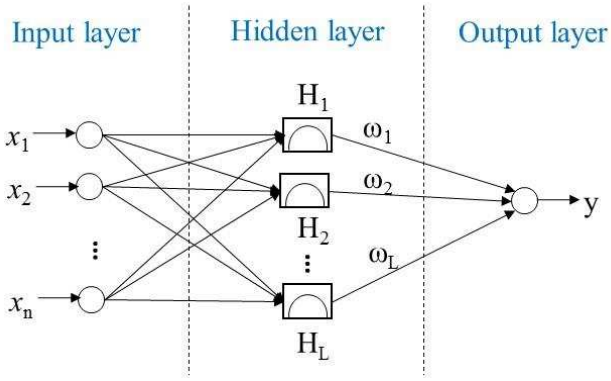

Fig. 3. Structure of an RBF-ANN.

D. SVM

SVM was developed by Vapnik in 1995 to solve the classification problem based on the statistic learning theory and structural risk minimization [27]. Since then, this method has been extended to the domain of regression and prediction problems [28]. As shown in Fig. 4, the input vector x is first mapped into an L-dimensional feature space using transfer functions and then a linear model is constructed in this feature space.

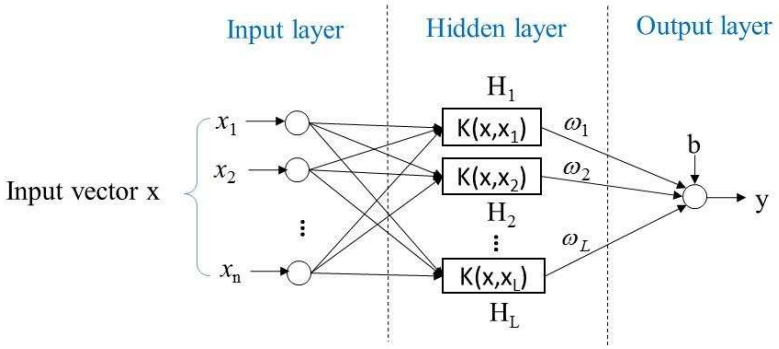

Fig. 4. Structure of an SVM.

The linear model in the feature space is given by

$$y = \omega x + b \tag{4}$$

where ω=(ω_1, ω_2,…, ω_L) is the weight vector and b is the bias term.

Regression estimates can be obtained by minimizing the empirical risk on the training data. SVM regression performs a linear regression in the high dimensional feature space using ε-insensitive loss and tends to reduce the model complexity by minimizing $\|\omega\|^2$. This can be described by introducing slack variables ξ_i and ξ_i' (i=1,2,…,m) to measure the deviation of training samples (X*, D) outside ε-insensitive zone. X*=(x^1, x^2,…, x^m) represents m input vectors of training samples and D=(d_1,d_2, …, d_m) is the corresponding desired output. Thus, the optimization problem can be formulated as

$$\Phi = \min \frac{1}{2}\|\omega\|^2 + C\sum_{i=1}^{m}(\xi_i + \xi_i') \quad (5)$$

where m is the number of training samples. C is a positive constant as a regularization parameter that allows tuning the tradeoff between the flatness of the function and the tolerance of deviations larger than ε (a constant).

Minimize the risk functional of Equation (5) subject to the following constraints:

$$d_i - y_i \le \varepsilon + \xi_i \quad (6)$$

$$y_i - d_i \le \varepsilon + \xi_i' \quad (7)$$

$$\xi_i \ge 0 \quad (8)$$

$$\xi_i' \ge 0 \quad (9)$$

Equation (4) can be transformed into a dual problem and solved by Lagrange functional.

$$y = \sum_{i=1}^{L}(\alpha_i - \alpha_i^*)\cdot K(x, x_i) + b \quad (10)$$

where α_i and α_i^* are Lagrange multipliers and K(x, x_i) is a kernel function.

There are some optional kernel functions for SVM such as linear, polynomial, radial basis function and sigmoid function. One of the most widely-used kernel functions is the radial basis function. The final product of a training process in the SVM method can be presented by:

$$y_{SVM} = \sum_{i=1}^{L}(\alpha_i - \alpha_i^*)\cdot \exp(-\frac{1}{2\sigma^2}\|x - x_i\|^2) + b \quad (11)$$

E. GP

GP as an evolutionary computation technique is an extension of genetic algorithms and is widely applied to symbolic data mining (symbolic regression, classification and optimization) [29-31]. Unlike traditional regression analysis, GP based symbolic regression automatically evolves both

the structure and parameters of the mathematical model from the available data. Meanwhile, it is superior to other machine learning techniques due to the ability to generate an empirical mathematical equation without assuming prior form of the existing relationships. In this study, multigene symbolic regression is applied to establish a model for two-phase flow measurement. The structure of a multigene symbolic regression model is shown in Fig. 5.

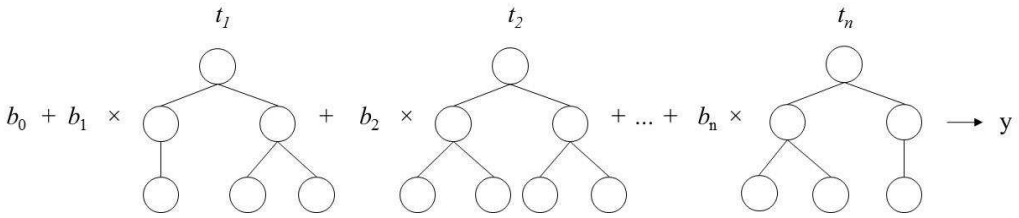

Fig. 5. Structure of a GP model.

The GP model can be regarded as a linear combination of lower-order nonlinear transformations of the input variables. The output y_{GP} is defined as a vector output of n trees modified by the bias term b_0 and scaling parameters b_1,…, b_n:

$$y_{GP} = b_0 + b_1 t_1 + ... + b_n t_n \tag{12}$$

where t_i (i=1,…, n) is the (m×1) vector of outputs from the i^{th} tree comprising a multigene individual.

The evolutionary process starts with initial population by creating individuals containing GP trees with different genes generated randomly. The evolutionary process continues with an evaluation of the fitness of the new population, two-point high-level crossover to acquire and delete genes and low-level crossover on sub-trees. Then the created trees replace the parent trees or the unaltered individual in the next generation through mutation operators. The best program that appeared in any generation, the best-so-far solution, defines the output of the GP algorithm [30].

III. EXPERIMENTAL RESULTS AND DISCUSSION

A. Test Rig and Experimental Conditions

Fig. 6 shows the schematic of the two-phase flow test rig that was used in this study. The measurement data obtained on this rig and subsequent conclusions drawn from the data are expected to be transportable to other gas-liquid two-phase flow conditions. The gas flow is set to enter to the liquid flow through a by-pass on the pipe. The liquid mass flowrate is controlled by adjusting the pump frequency from 15 to 80%. The gas flowrate is varied by adjusting the opening of the valve in a gas flow controller. Two independent Coriolis flowmeters (KROHNE OPTIMASS 6400 S25 and Bronkhorst mini CORI-FLOW M15) were installed before the mixer to provide references for the individual mass flow rates of the liquid and gas phases respectively. Both reference meters' measurement uncertainties under single-phase conditions were verified according to the manufacturer's technical specification. In the downstream, two additional Coriolis flowmeters (see Fig. 7) of the same type as the liquid reference meter were installed in the vertical and horizontal test sections, respectively. These are the meters under test to assess the performance of ANN, SVM and GP models under two-phase flow conditions. In view of the effects of gravity and buoyancy on two-phase fluid, both horizontal and vertical installations of the meters are considered. A DP transducer was used to record the DP value across each flowmeter under test.

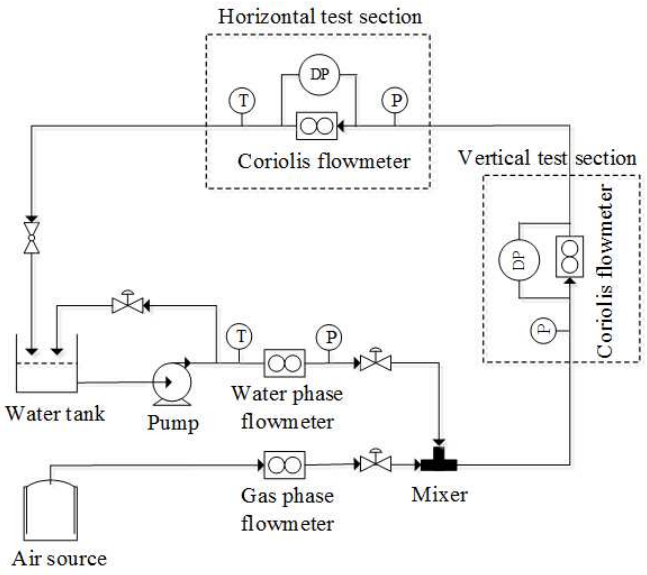

Fig. 6. Schematic of the two-phase flow test rig.

Fig. 7 Photo of the test Coriolis flowmeters on 1-inch pipelines.

The data logging frequencies, as set in the data loggers for the mass flowrate, density, damping and DP, are 50Hz, 10Hz, 2Hz and 20Hz, respectably. Each parameter was logged over a period of 100s with a time averaged value generated under each experimental condition. Gas volume fraction α is defined and calculated as follows

$$\alpha = \frac{q_{v,g}}{q_{v,l} + q_{v,g}} \times 100\% \tag{13}$$

where $q_{v,g}$ and $q_{v,l}$ are the calculated volume flowrates of gas and liquid phases from the reference flow meters and the temperature and pressure in the upstream of the horizontal test meter.

Density drop is determined from the density of the liquid flow (ρ_l) and the apparent density (ρ) from the Coriolis flowmeter under test:

$$d = \frac{\rho_l - \rho}{\rho_l} \times 100\% \tag{14}$$

Two series of experimental tests, Tests I and Tests II, were conducted for the liquid mass flow rate ranging from 700 kg/h to 14500 kg/h and gas volume fraction from 0 to 30%. The fluid temperature during the tests was around 20°C. For the purpose of ANN training, 237 data sets were collected from Tests I while 24 data sets recorded from Tests II for testing the performance of the data driven models.

B. Analysis of original errors

The typical original mass flow errors of the Coriolis flowmeters in Tests I are plotted in Fig. 8. The Coriolis flowmeter on the vertical section gives negative errors at flowrates below 4000 kg/h. At a higher flowrate (>5500 kg/h), the mass flow errors become positive and crossing the zero line and then return to negative errors again along with increasing entrained gas. This is believed to be due to the flow regime effects on the fluid-tube coupling system at different flowrates. At a lower flowrate (< 2000 kg/h), the flow was nearly slug flow as observed during the test while the flow regime became gradually dispersed bubbly flow as the flowrate and entrained gas increase. For the Coriolis flowmeter on the horizontal pipeline, the range of mass flow errors is different from that on the vertical pipeline most likely due to the effects of gravity and buoyancy on the flow regime. Positive errors occur at mass flowrates of 700 kg/h and 1000 kg/h when the gas volume fraction below 6%. By comparing the mass flow errors at the same flowrate in Fig. 8 and Fig. 9, the errors are generally reproducible for the same installation and thanks to the new-generation flow transmitter [32]. For the test dataset, Test II includes some experimental data which were collected at different flowrates from those in Test I. The new conditions as in Test II

which were conducted on a different day and obtained under different flowrate from Test I are useful to assess the models' generalization capability and reproducibility.

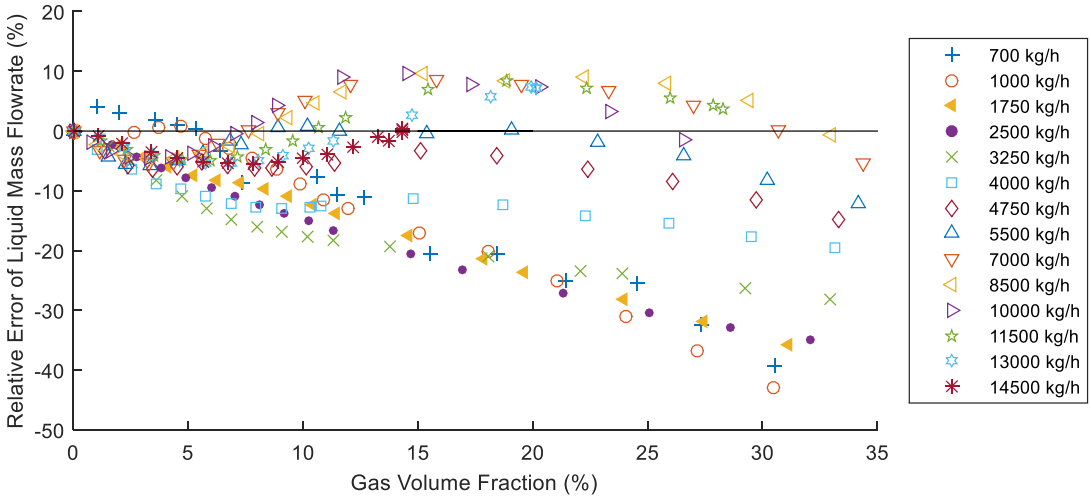

(a) Horizontal pipeline

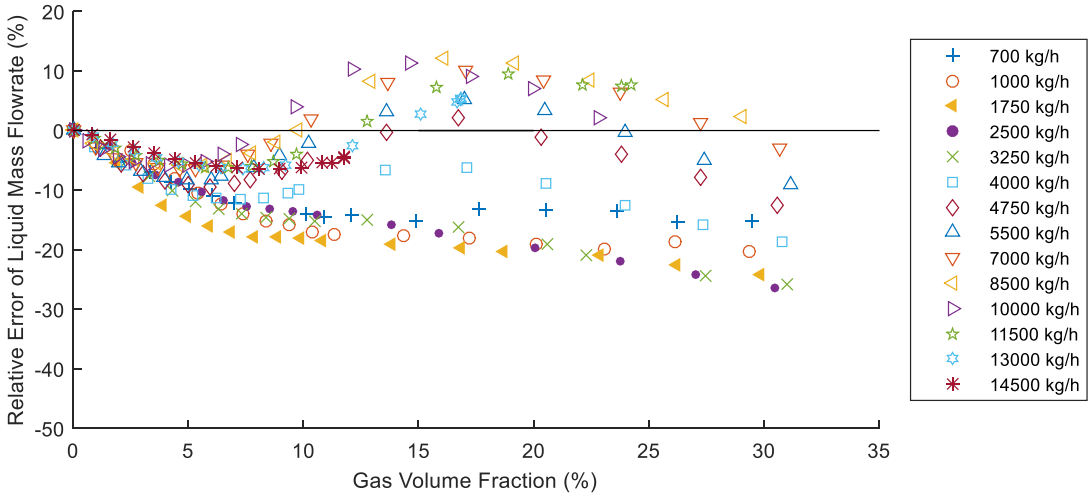

(b) Vertical pipeline

Fig. 8. Original errors of the liquid mass flowrate from Test I.

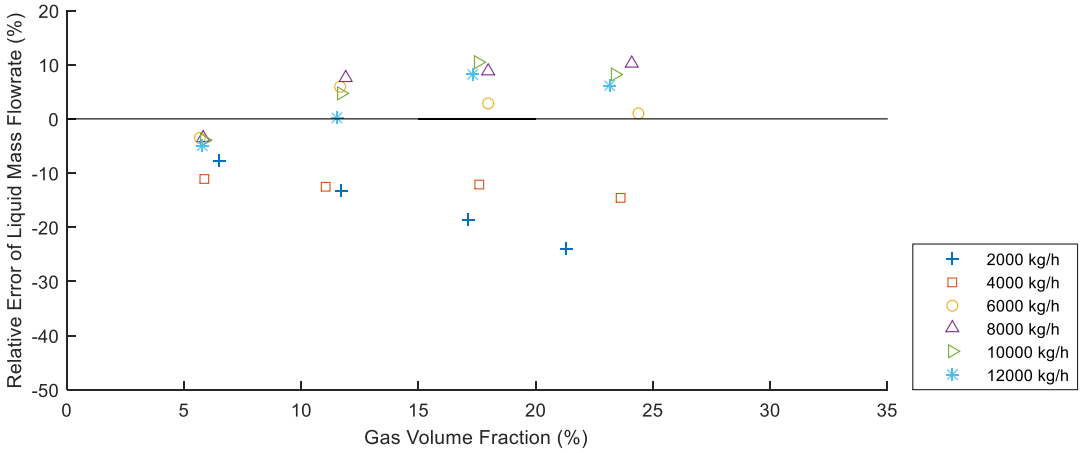

(a) Horizontal pipeline

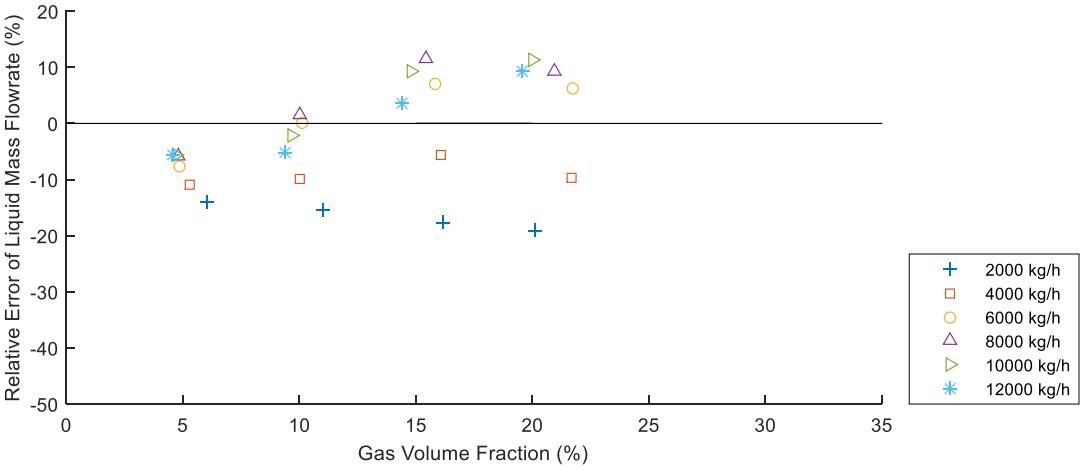

(b) Vertical pipeline

Fig. 9. Original errors of the liquid mass flowrate from Test II.

Fig. 10 depicts the distribution of the relative errors of the measured liquid mass flowrate on both horizontal and vertical pipelines. Each color (blue or green) in the figure represents training or test datasets respectively. The Coriolis flowmeter on the horizontal pipeline yields the liquid mass flowrate with a relative error between -41% and 9% whilst the meter on the vertical pipeline gives an error from -25% to 11%. The difference in errors between the vertical and horizontal installations is due to the fact that the bubbles in a vertical flow are distributed evenly in the pipe

cross section due to the effect of gravity, resulting in less interruptions on the tube vibration inside the Coriolis flowmeter and hence different errors.

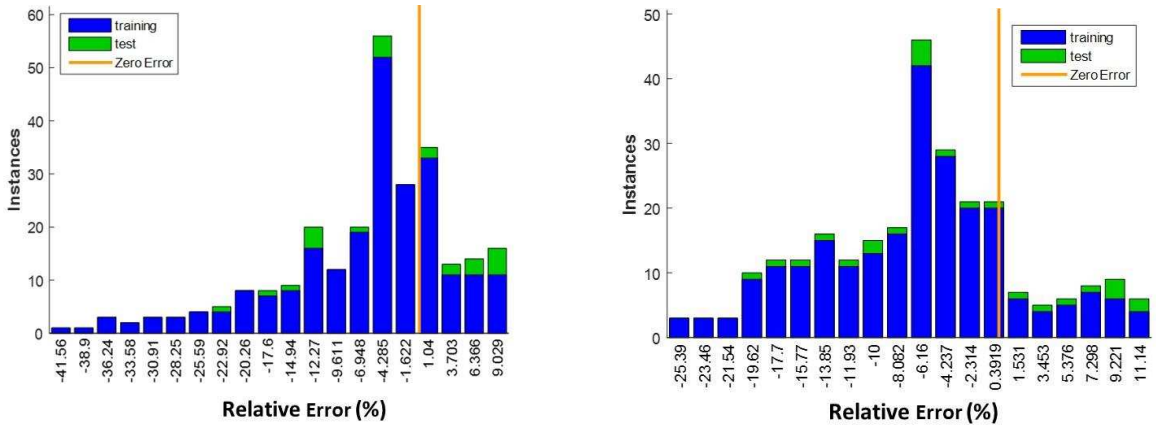

(a) Horizontal pipeline (b) Vertical pipeline

Fig. 10. Relative error histogram of the measured liquid mass flowrate.

C. Analysis of parametric dependence

There are three important parameters from a Coriolis flowmeter, including observed density drop, apparent mass flowrate and damping. The DP value from the DP transducer is also included as a potential input variable in this study. The apparent mass flowrate from a Coriolis flowmeter and the DP value across the meter correlates strongly with the liquid mass flowrate under two-phase conditions. In addition, when gas entrains in the liquid flow, a rapid rise in damping occurs for the fluid-conveying tube and the mixture density also deviates from the liquid density. This physical background for the fluid-tube coupling system determines that these four input variables are more important than other variables. There exists strong nonlinearities between the outputs of a Coriolis flowmeter and the flowrate being measured under two-phase flow conditions, as observed by other researchers [12, 13]. Such nonlinearities are also evident in Fig.8.

In order to investigate the parametric dependence of individual input parameters and the combined effect of multiple parameters on the output of a data model, Partial Mutual Information

(PMI) is utilized to measure the partial dependence between a potential input variable and the output, conditional on any inputs that have already been selected. The variable with the highest PMI score is added to the input set, if the Akaike information criterion (AIC) value decreases as a result from the inclusion of this variable. Detailed definitions of PMI and AIC are available in [19, 20]. Suppose variables x_1, x_2, x_3 and x_4 represent observed density drop, apparent mass flowrate, damping and DP, respectively, the variable selection procedures for the models for correcting the liquid mass flowrate and predicting the gas volume fraction are summarized in Tables I and II. H-L and V-L represent the models established for horizontal and vertical pipelines, respectively, to correct the liquid mass flowrate, while H-G and V-G stand for the models for horizontal and vertical pipelines to predict the gas volume fraction, respectively. The selection sequence also represents the sensitivity level of each variable to the desired output. For the liquid mass flowrate, x_2 (apparent mass flowrate) has more significant effect on the liquid mass flowrate. The coefficient of determination, R^2, indicates the goodness of fit. A combination of the four variables gives the highest R^2, which illustrates the combined effect of the variables is more significant than that of an individual variable on the output. For the models used for predicting the gas volume fraction, x_1 (observed density drop), plays a more important part than other variables. Variable x_4 (DP) is not used in Models H-G and V-G since the AIC value becomes increasing and R^2 is reducing with the inclusion of x_4. As a result of these variable selection procedures, the models for correcting the liquid mass flowrate accept the four input variables (observed density drop, apparent mass flowrate, damping and DP) and three variables (observed density drop, apparent mass flowrate and damping) are taken as the inputs to the models for predicting the gas volume fraction.

Table I Variable selection procedures for models H-L and V-L.

Step	Model H-L			Model V-L		
	Variable	AIC	R^2	Variable	AIC	R^2
I	x_2	-1030	0.9795	x_2	-1027	0.9793
II	x_3	-971	0.9757	x_4	-1032	0.9797
III	x_4	-1040	0.9814	x_3	-1085	0.9842
IV	x_1	-1161	0.9886	x_1	-1200	0.9901

Table II Variable selection procedures for models H-G and V-G.

Step	Model H-G			Model V-G		
	Variable	AIC	R^2	Variable	AIC	R^2
I	x_1	-669.3	0.921	x_1	-485.8	0.843
II	x_3	-743.3	0.9434	x_3	-668.1	0.9248
III	x_2	-745.9	0.9456	x_2	-691.1	0.9334
IV	x_4	-727.4	0.9415	x_4	-669.2	0.9272

D. Performance of the BP-ANN

The BP-ANN model is established through training with dataset I and tested with dataset II. For each installation condition a separate model is established for the correction of the measured liquid mass flowrate and the prediction of gas volume fraction. The inputs of the BP-ANN for liquid mass flowrate correction include four variables, i.e. observed density drop, apparent mass flowrate, damping and DP. The inputs of the BP-ANN for gas volume fraction prediction include observed density drop, apparent mass flowrate and DP. The number of neurons (L) in the hidden layer is determined using the equations below, as proposed by Hecht-Nielson and Rogers and Dowla [33]:

$$L \leq 2n+1 \tag{15}$$

$$L \le \frac{m}{n+1} \tag{16}$$

where n and m are the numbers of input variables and training samples, respectively. However, equations (15) and (16) give only the range of L for BP-ANN models. The exact L for a model can be selected by a trial-and-error method to compromise between minimizing errors and achieving good generalization capability. The output layer has one neuron for each model since there is only one output variable.

The BP-ANN transfer function between the input and hidden layers is hyperbolic tangent sigmoid transfer function. The pure linear function is taken as the transfer function connecting the hidden layer to the output layer. The training function is Bayesian regularization whilst the learning function is gradient descent with momentum weight and bias learning function. Training stops when the maximum number of epochs is reached or the performance is minimized to the goal. In this study, NRMSE (Normalized Root-Mean-Square Error) is used to assess the performance of a data driven model, which is defined as

$$\mathrm{NRMSE} = \frac{1}{\bar{y}} \sqrt{\frac{1}{m} \sum_{i=1}^{m} (y_i - \hat{y}_i)^2} \tag{17}$$

where y_i is the reference mass flow rate of the liquid phase or gas volume fraction, $\bar{y}$ the mean of y_i, $\hat{y}_i$ the corrected mass flow rate or predicted gas volume fraction from the data driven model accordingly, and m the number of samples used.

As the weights and biases between the neurons are initialized randomly, a different BP-ANN is obtained for each training, resulting in different performance. A preliminary study of averaging NRMSE of more than 200 BP-ANNs did not show any noticeable difference. Therefore, in order to minimize the effect of random initialization of an ANN, the average NRMSE of 200 BP-ANNs

with the same structure is calculated to assess the effect of the hidden neurons on the performance of the ANN.

For the models for liquid mass flowrate correction, the number of neurons in the hidden layer is set from 4 to 9 as per equations (15) and (16). The NRMSE values of the BP-ANNs are summarized in Fig. 11. The error bars indicate the maximum and minimum errors of 200 BP-ANNs for the same structure. In view of the errors on both training and test datasets, the BP-ANN with 7 neurons in the hidden layer performs better than other structures under both horizontal and vertical conditions. The BP-ANN used for gas volume fraction prediction has lower NRMSE when the number of the hidden neurons is 6.

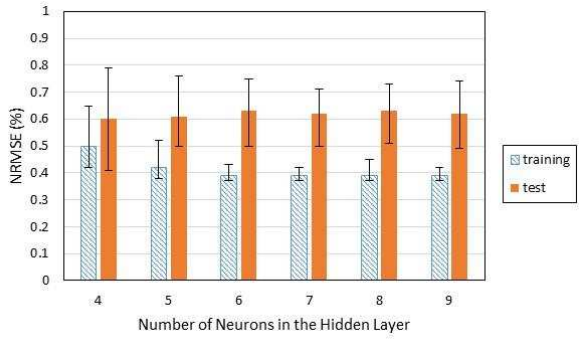

(a) BP-ANN: H-L

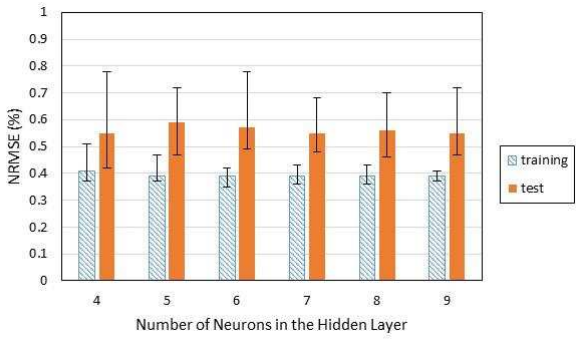

(b) BP-ANN: V-L

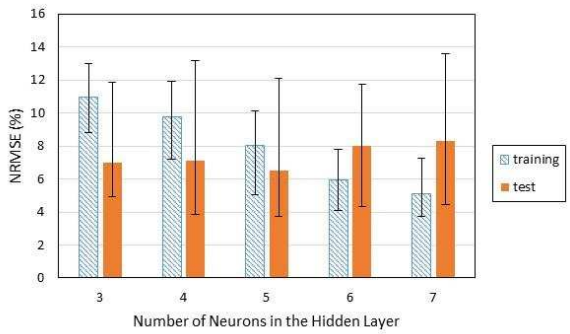

(c) BP-ANN: H-G

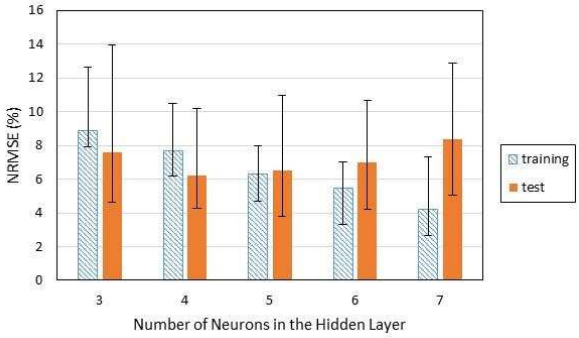

(d) BP-ANN: V-G

Fig. 11. Performace of BP-ANNs with differenct numbers of neurons in the hidden layer.

Once the structure of a BP-ANN is determined, the trained neural network which has the minimum error with the test dataset is selected. Fig. 12 shows the errors of the corrected liquid mass flowrate from the BP-ANNs. For the horizontal and vertical pipelines, the relative errors are mostly less than ±2% (the red dash lines in Fig. 12) with the training dataset except some larger errors at low flowrates of 700 kg/h and 1000 kg/h. This is very likely due to larger bubbles or slugs appearing in the flow tubes under low flowrate which affects the Coriolis flowmeter behaving differently from smaller bubbles. The trained BP-ANN has relatively larger errors at low flowrates and hence result in unsatisfactory performance with the test dataset under the same experimental conditions.

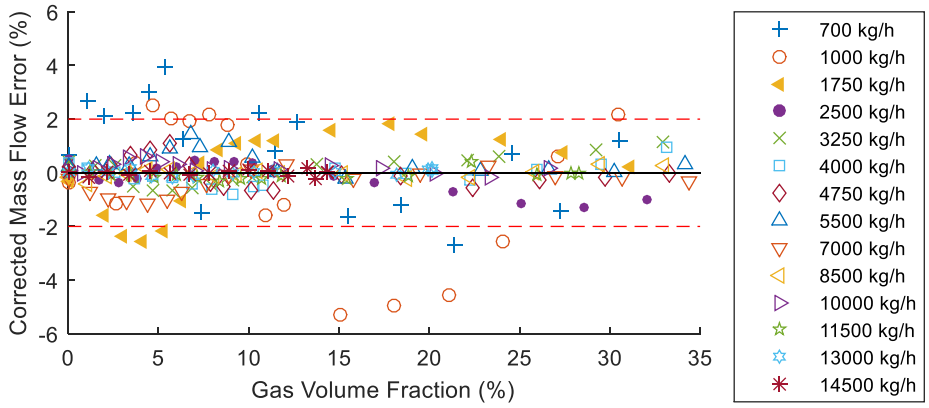

(a) Errors of the corrected mass flowrate on horizontal pipeline with training dataset

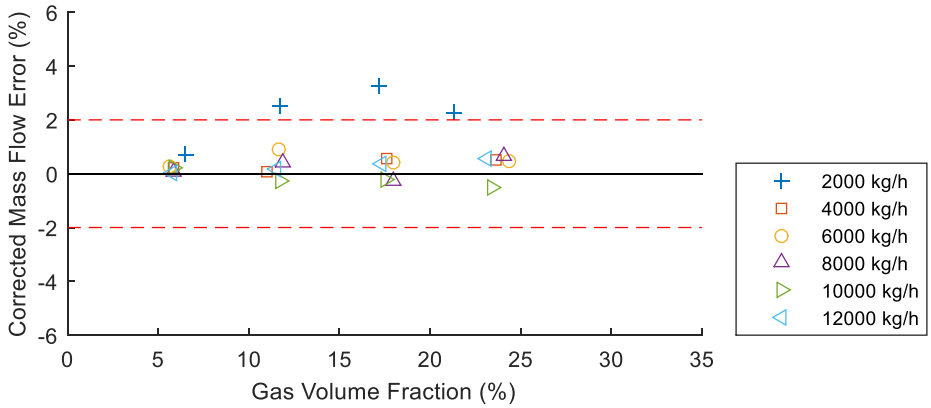

(b) Errors of the corrected mass flowrate on horizontal pipeline with test dataset

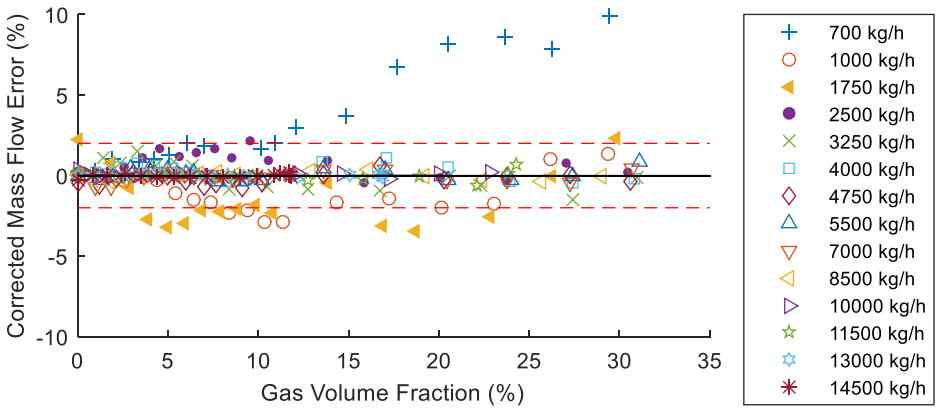

(c) Errors of the corrected mass flowrate on vertical pipeline with training dataset

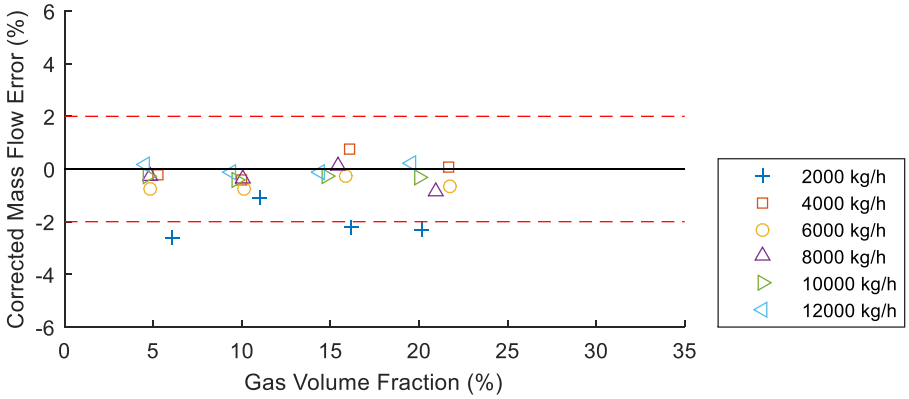

(d) Errors of the corrected mass flowrate on vertical pipeline with test dataset

Fig. 12. Errors of the corrected liquid mass flowrate from the trained BP-ANNs.

Since the gas volume fraction under the experimental conditions ranges from 0 to 30% and the intrinsic complexity of two-phase flow, the relative errors of the predicted gas volume fraction from the BP-ANNs are quite large when the gas volume fraction is below 5%. As the entrained gas increases, the errors from the training dataset are mostly within ±10% (the red dash lines in Fig. 13). For the test dataset, however, all the errors are less than ±10% on the vertical pipeline, even under the low flowrate conditions.

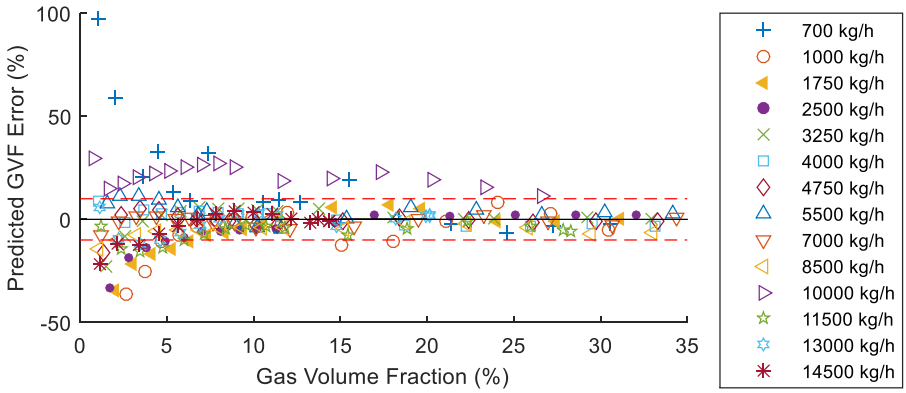

(a) Errors of the predicted gas volume fraction on horizontal pipeline with training dataset

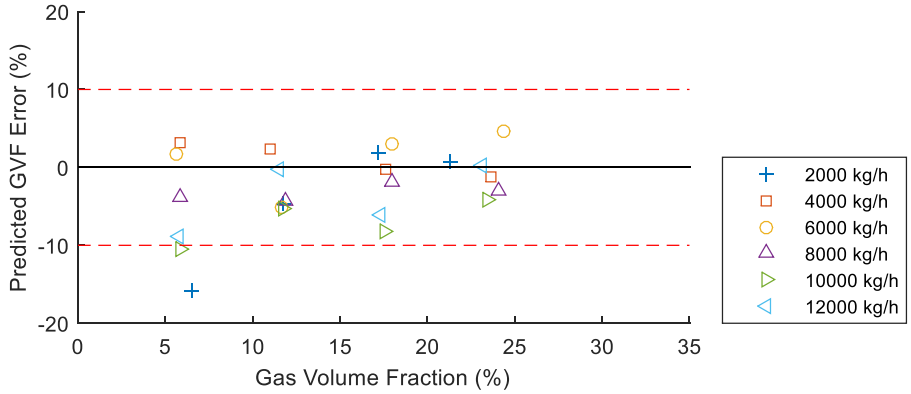

(b) Errors of the predicted gas volume fraction on horizontal pipeline with test dataset

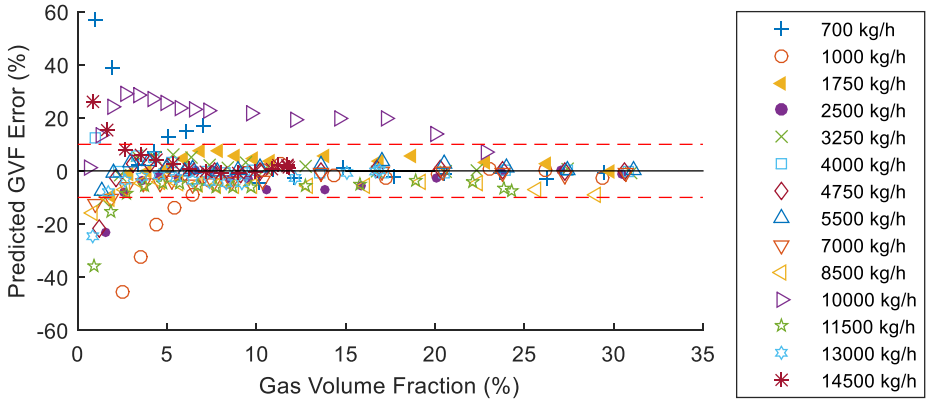

(c) Errors of the predicted gas volume fraction on vertical pipeline with training dataset

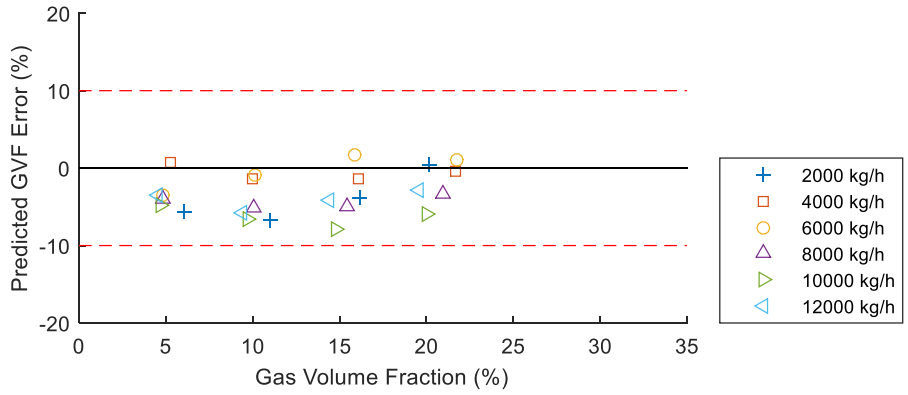

(d) Errors of the predicted gas volume fraction on vertical pipeline with test dataset

Fig. 13. Error of the predicted gas volume fraction from the trained BP-ANNs.

E. Performance of the RBF-ANN

Fig. 14 shows the relative errors of the corrected liquid mass flowrate from the RBF-ANNs. In order to achieve more accurate results with the test dataset, the RBF-ANN on the horizontal pipeline disregards the errors at lower flowrates (<2000 kg/h) and the network is trained to well fit higher flowrates (>4000 kg/h). Consequently, the errors at higher flowrates with the training dataset and the errors with the test dataset are reduced to ±1%. Due to the insignificant difference in the original errors between the lower and higher flowrates on the vertical pipeline, the RBF-ANN yields errors between ±2% with the training dataset and ±1% with the test dataset.

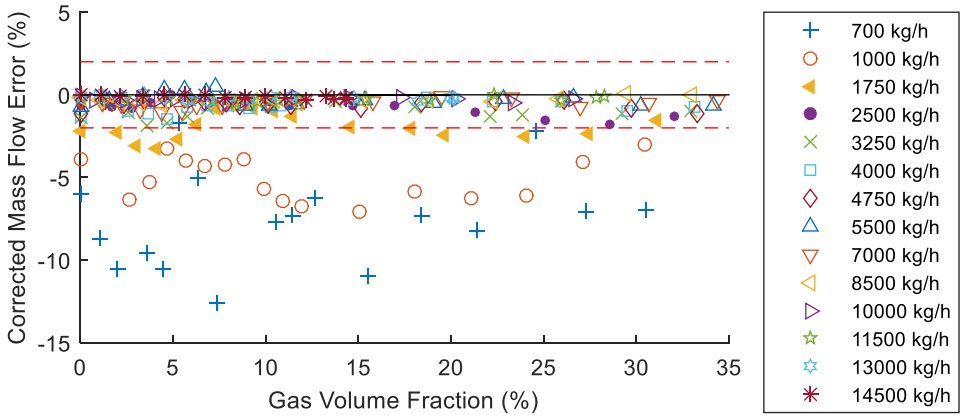

(a) Errors of the corrected mass flowrate on horizontal pipeline with training dataset

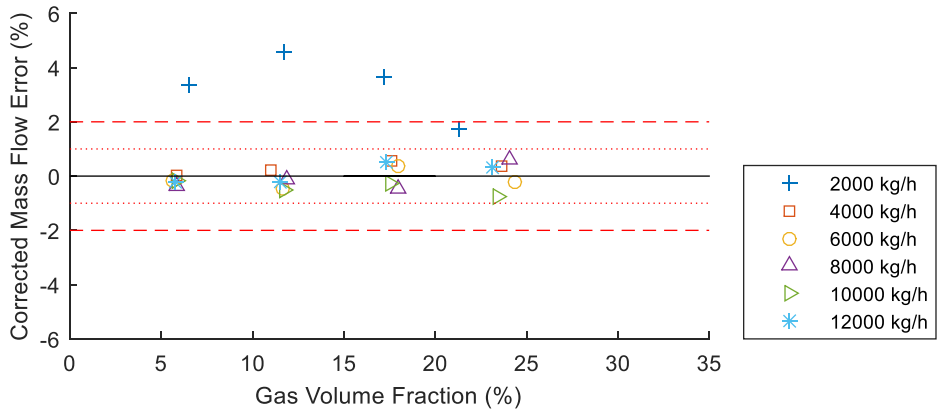

(b) Errors of the corrected mass flowrate on horizontal pipeline with test dataset

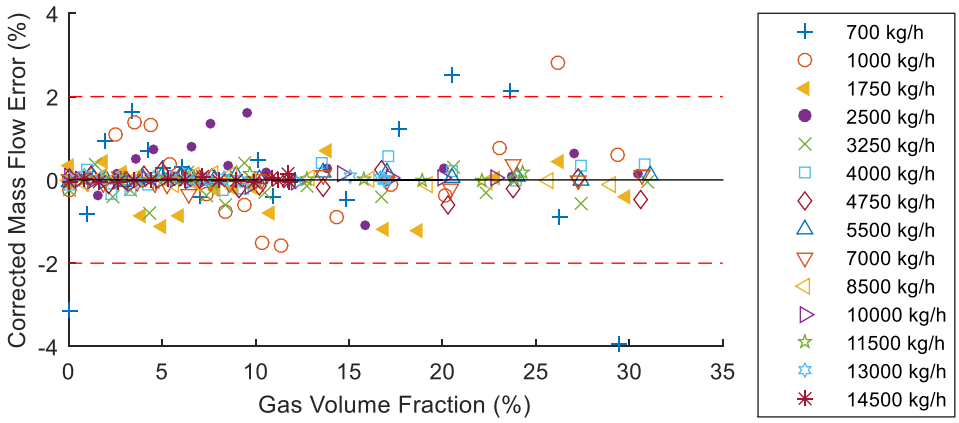

(c) Errors of the corrected mass flowrate on vertical pipeline with training dataset

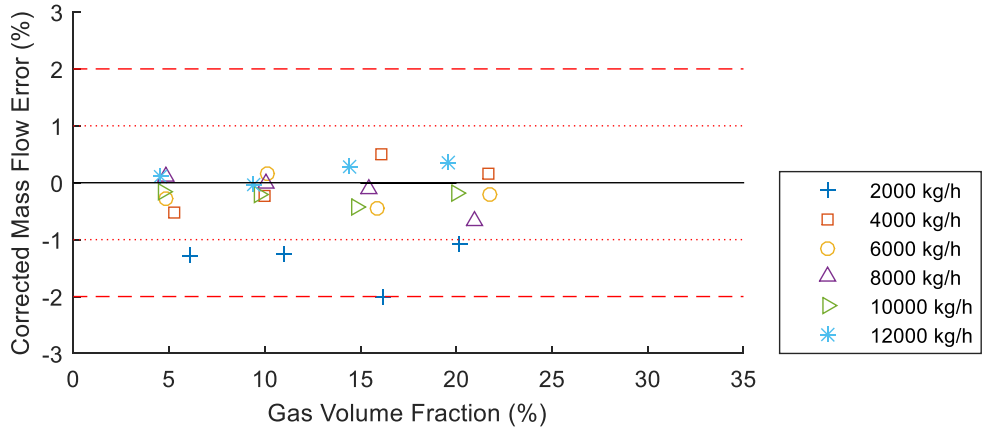

(d) Errors of the corrected mass flowrate on vertical pipeline with test dataset

Fig. 14. Errors of the corrected liquid mass flowrate from the RBF-ANNs.

As shown in Fig. 15, the RBF-ANN for gas volume fraction prediction outperforms significantly the BP-ANN, particularly under the low entrained gas. When the gas volume fraction is below 5%, the maximum relative errors from RBF-ANNs on both horizontal and vertical pipelines are around ±30%. The rest errors with the training dataset are well within ±10%. The relative errors from the test dataset are almost less than ±10%, except at the flowrate of 1000 kg/h on the horizontal pipeline. This is probably due to the fact that the samples at 1000 kg/h flow rate are far away from the centre vectors in the network.

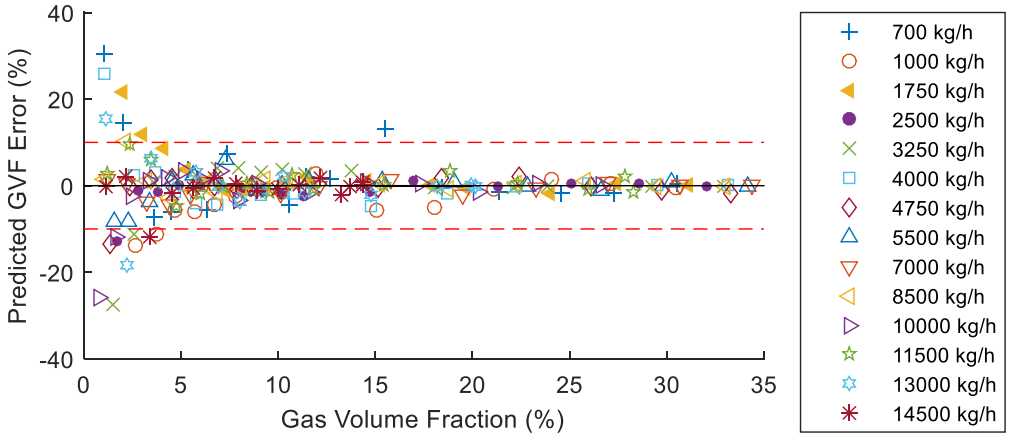

(a) Errors of the predicted gas volume fraction on horizontal pipeline with training dataset

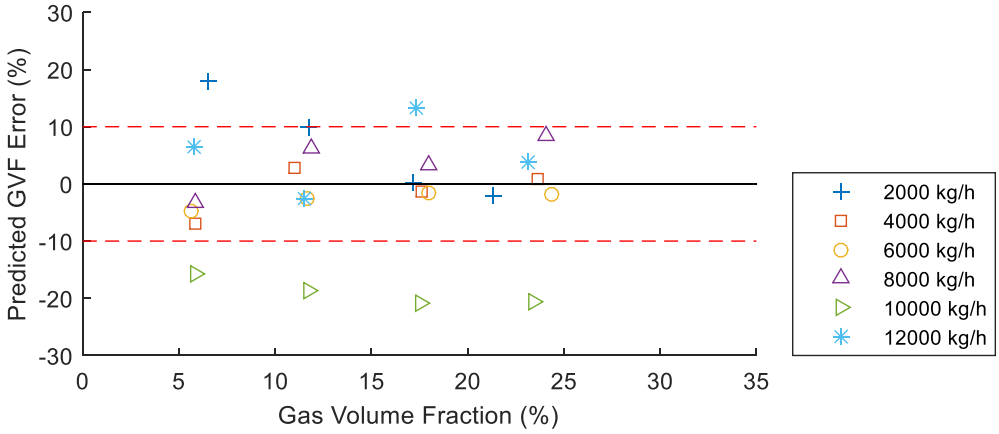

(b) Errors of the predicted gas volume fraction on horizontal pipeline with test dataset

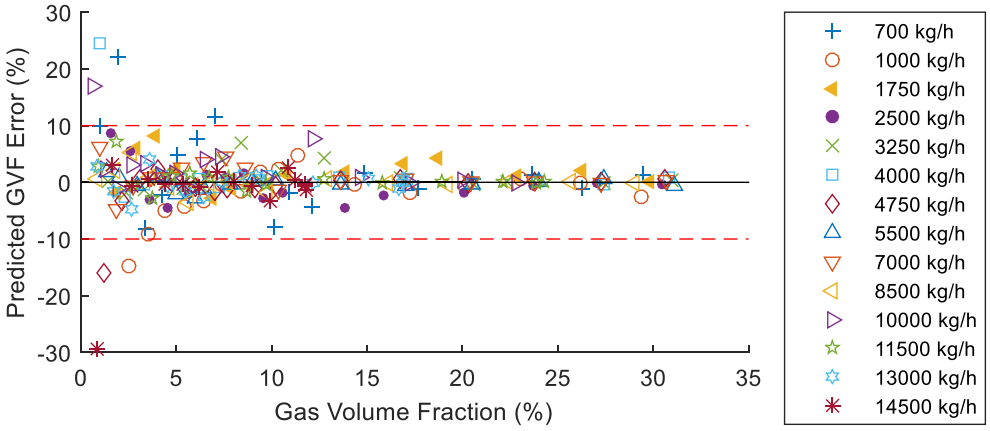

(c) Errors of the predicted gas volume fraction on vertical pipeline with training dataset

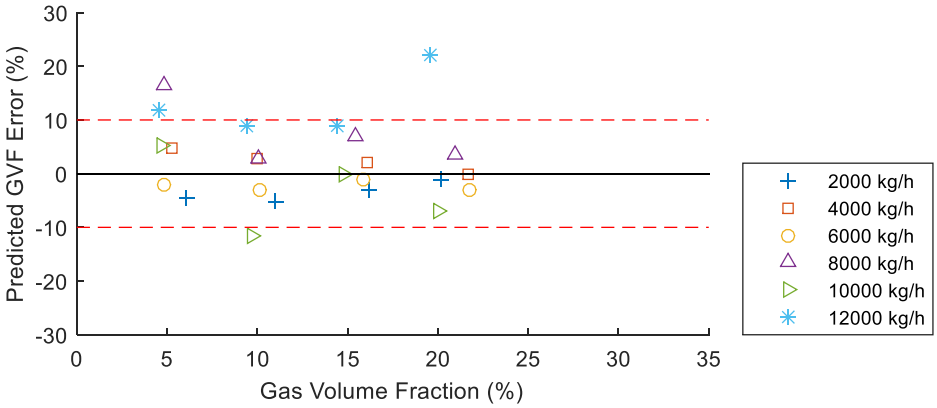

(d) Errors of the ppredicted gas volume fraction on vertical pipeline with test dataset

Fig. 15. Errors of the predicted gas volume fraction from the RBF-ANNs.

F. Performance of the SVM

SVM models are also established for both installation conditions. An important difference between the SVM and ANN models is that the SVM leads to a unique deterministic model for each dataset while ANNs depend on a random initial choice of synaptic weights and cannot produce the fixed results. Through a direct comparison of the performances of SVM between the four kinds of kernel function (Table III), we know that the SVM with radial basis function generates the smallest NRMSE among the four models.

Table III NRMSE of SVM with different kernel functions

Model	Data set 1				Data set 2			
	Linear	Polynomial	Radial basis function	Sigmoid	Linear	Polynomial	Radial basis function	Sigmoid
H-L	5.62%	11.12%	0.11%	889.50	7.44%	10.97%	0.58%	738.32
V-L	6.32%	10.33%	0.10%	911.90	9.39%	11.42%	0.57%	777.32
H-G	21.37%	28.37%	3.44%	606.58	2.6%	5.68%	3.29%	138.03
V-G	27.27%	34.08%	2.16%	683.13	3.71%	6.78%	3.2%	171.56

From Fig. 16 (a) and (c), the SVM model performs well to fit with training data and limit the relative errors on horizontal and vertical pipelines to ±1% or less, except some points at 700 kg/h and 1000 kg/h, which is a common problem for the ANN and SVM models. The generalization ability of the SVM model is proven as shown in Fig. 16 (b) and (d). Most errors from the SVM models with the test data are reduced to ±1%.

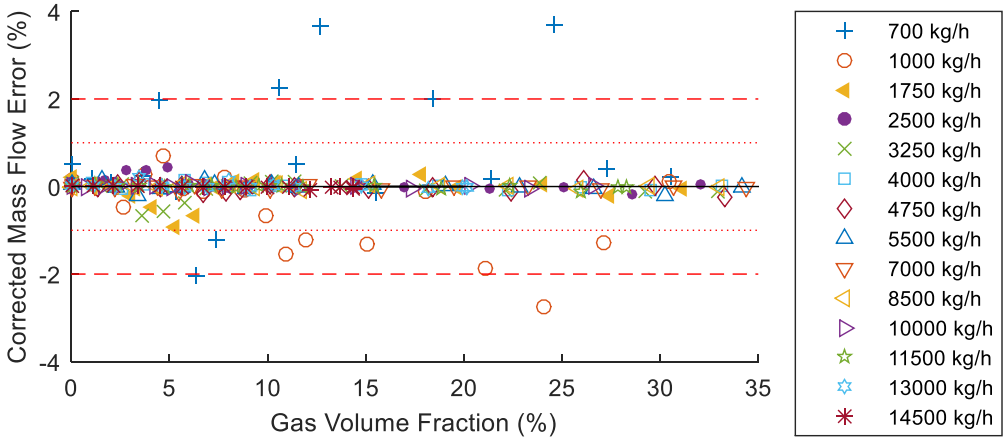

(a) Errors of the corrected mass flowrate on horizontal pipeline with training dataset

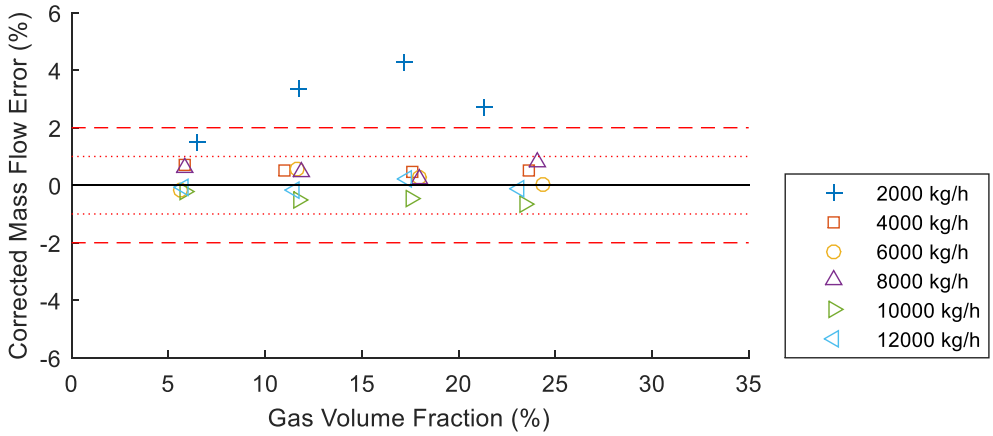

(b) Errors of the corrected mass flowrate on horizontal pipeline with test dataset

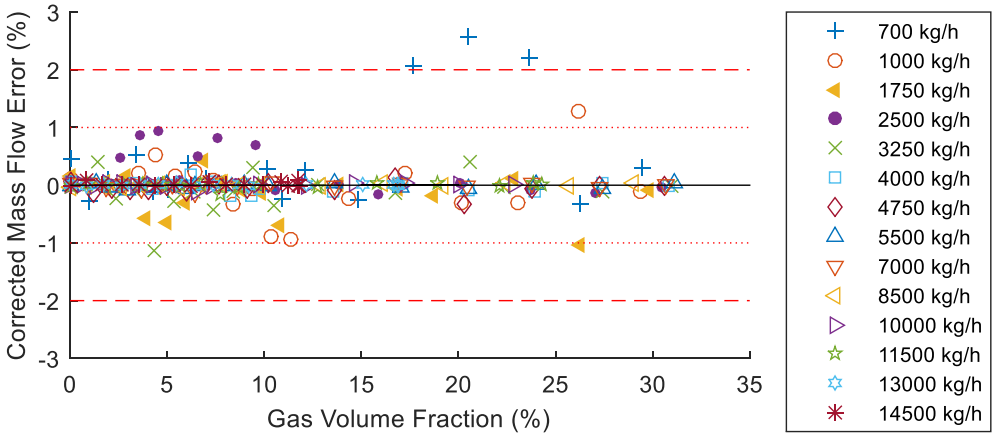

(c) Errors of the corrected mass flowrate on vertical pipeline with training dataset

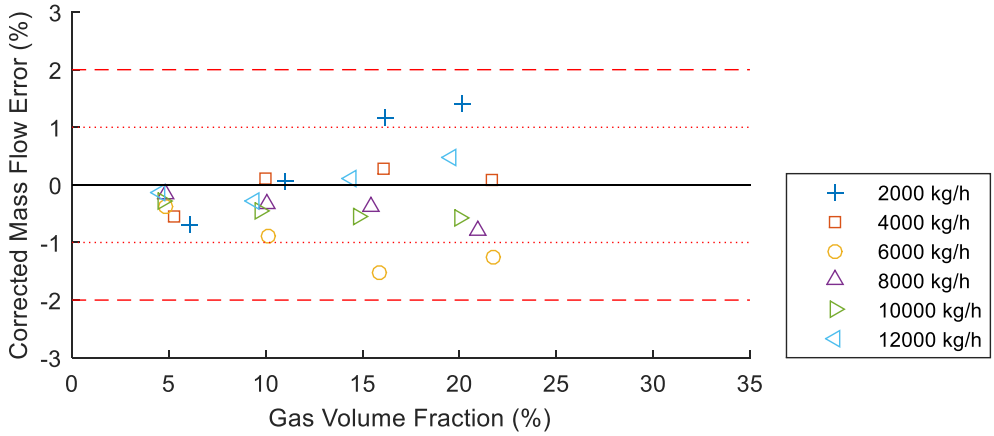

(d) Errors of the corrected mass flowrate on vertical pipeline with test dataset

Fig. 16. Errors of the corrected liquid mass flowrate error from the SVMs.

Fig. 17 indicates that, for gas volume fraction prediction, a less number of points from the SVM models have an error beyond ±10% with the training dataset. Since the kernel function used in the SVM models is radial basis function, the performance of the SVM models has the common problem with the RBF-ANN. The relative errors in the predicted gas volume fraction with the test dataset at the flowrate of 1000 kg/h is larger than other test data.

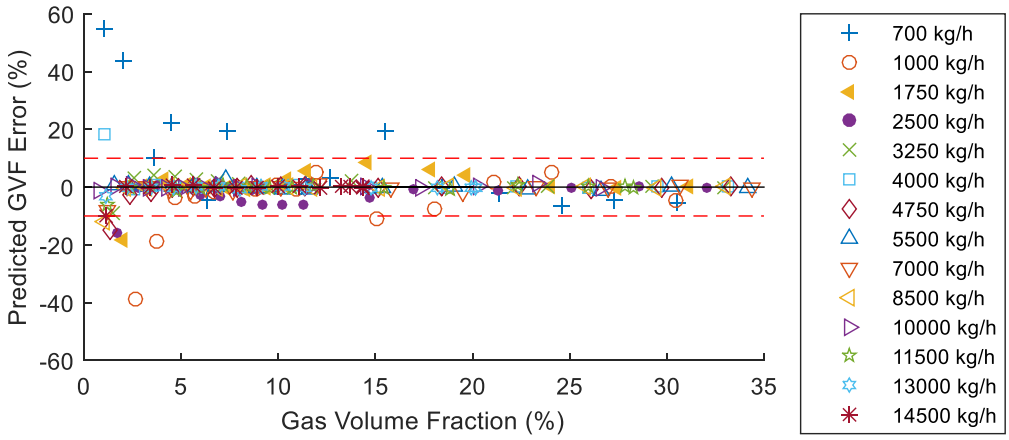

(a) Errors of the predicted gas volume fraction on horizontal pipeline with training dataset

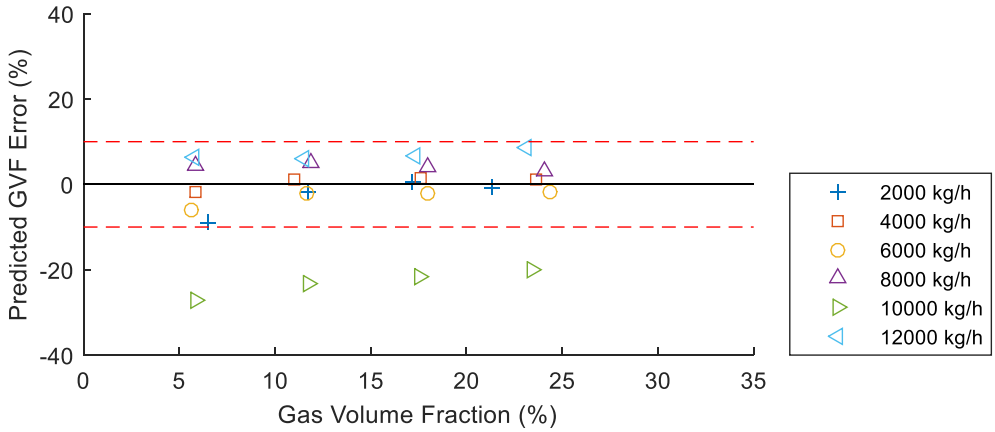

(b) Errors of the predicted gas volume fraction on horizontal pipeline with test dataset

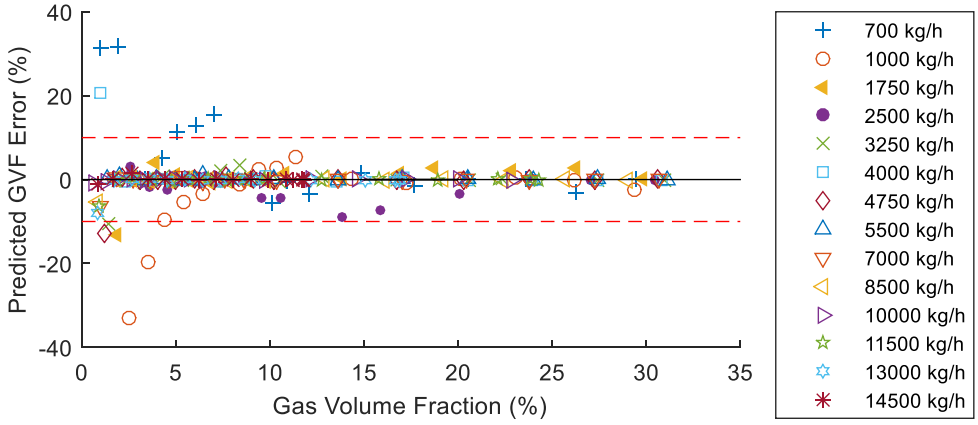

(c) Errors of the predicted gas volume fraction on vertical pipeline with training dataset

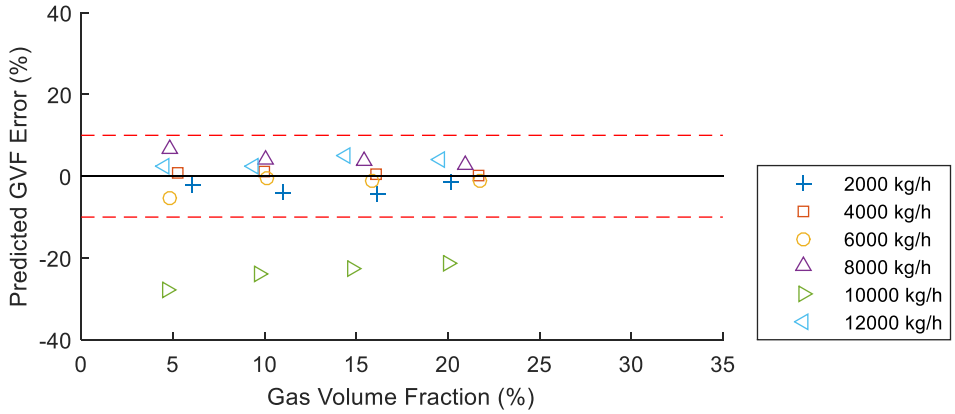

(d) Errors of the predicted gas volume fraction on vertical pipeline with test dataset

Fig. 17. Errors of the predicted gas volume fraction from the SVMs.

G. Performance of the GP

Four GP models are established in this study for correcting the liquid mass flowrate and predicting the gas volume fraction, respectively, for horizontal and vertical installations of Coriolis flowmeters. The parameters that were set in the GP algorithms include: population size 250, tournament size 25, elitism 0.7, maximum number of genes allowed in an individual 6, function set {×, -, +, tanh, mult3, add3}, terminal sets {x_1, x_2, x_3, x_4} for models H-L and V-L and {x_1, x_2, x_3} for models H-G and V-G.

The GP-based formulations for the four models are given below:

$$y_{H-L} = 0.994\,x_2 - 2633\,x_1 + 4300\,\tanh(x_1)\tanh(x_3) + 13.2\,x_1x_4 + 0.00571\,x_2x_3 - 0.0995\,x_2x_3\tanh(x_1) + 62.4 \quad (18)$$

$$y_{V-L} = x_2 + 57.6x_3 - 0.161\,x_4 + 29.8x_1x_4 + 871\tanh(x_3^2x_4)\tanh(x_1) - 0.00913\,x_4(x_3 + x_1x_4) - 0.122\,x_1x_2x_3 + 32.5 \quad (19)$$

$$y_{H-G} = 0.783\,x_1 + 1.6e^{-6}x_2 + 0.00278\,x_3 - 0.114\,x_1x_3 + 0.159\,x_1^2x_3 + 6.82e^{-5}x_3^3 - 0.0182 \quad (20)$$

$$y_{V-G} = 1.01x_1 - 5.49e^{-7}x_2 - 0.0217\,x_3 - 2.74e^{-7}\tanh(x_1) - 1.05e^{-4}x_1x_2 + 2.74e^{-6}x_2x_3 + 0.00253\,x_1x_3^2 - 1.05e^{-4}x_1^2x_3 - 2.74e^{-7}x_1x_2x_3 + 0.00587 \quad (21)$$

The errors of the corrected mass flowrate on the training dataset using GP are higher by -15% and 25%, respectively, under horizontal and vertical installations (Fig. 18 (a) and (c)), which results in larger errors on the test dataset (Fig. 18 (b) and (d)). As can be seen that larger errors normally occur at low flowrates, which indicates that the GP models are unable to approximate all the data.

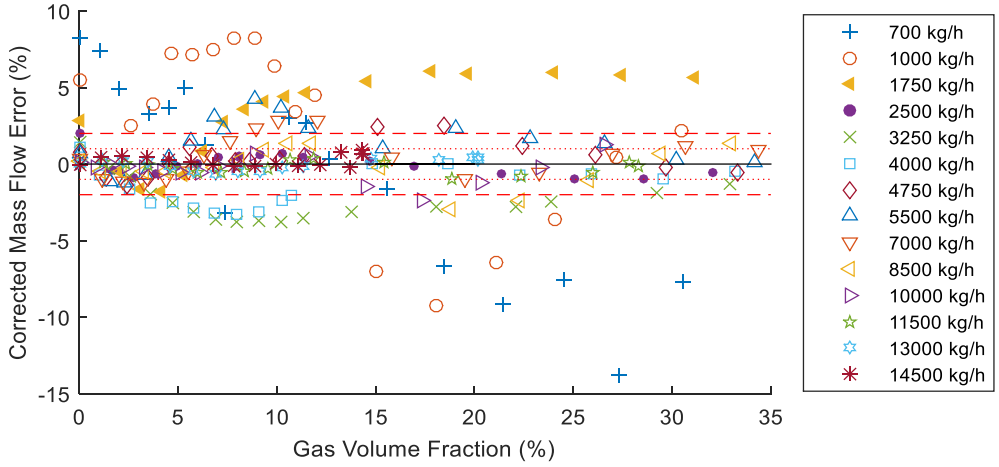

(a) Errors of the corrected mass flowrate on horizontal pipeline with training dataset

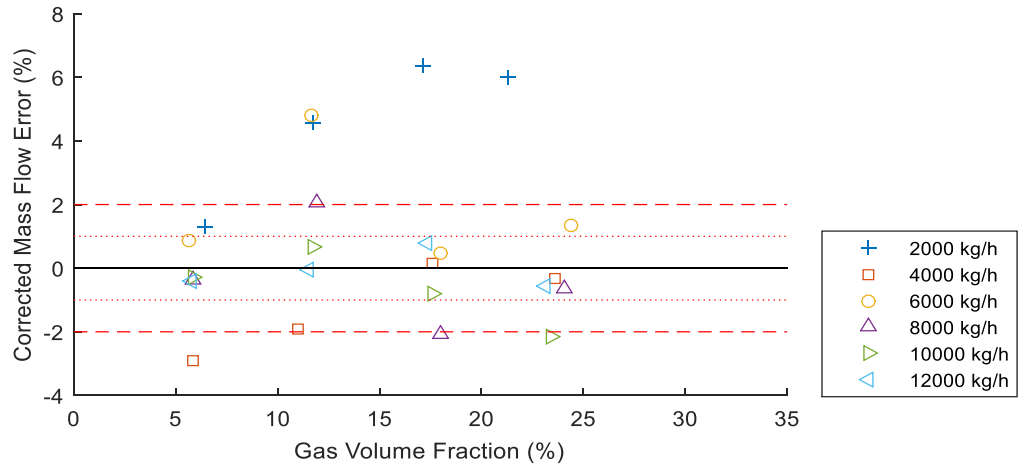

(b) Errors of the corrected mass flowrate on horizontal pipeline with test dataset

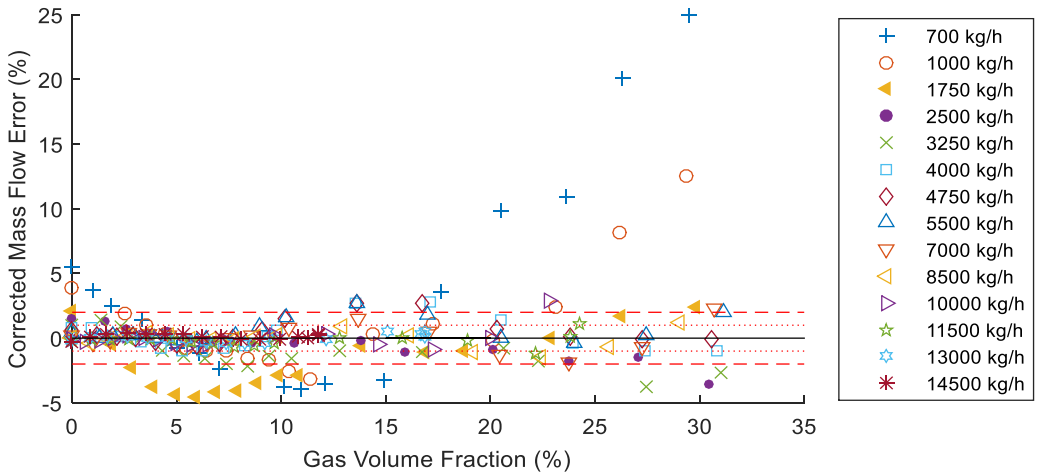

(c) Errors of the corrected mass flowrate on vertical pipeline with training dataset

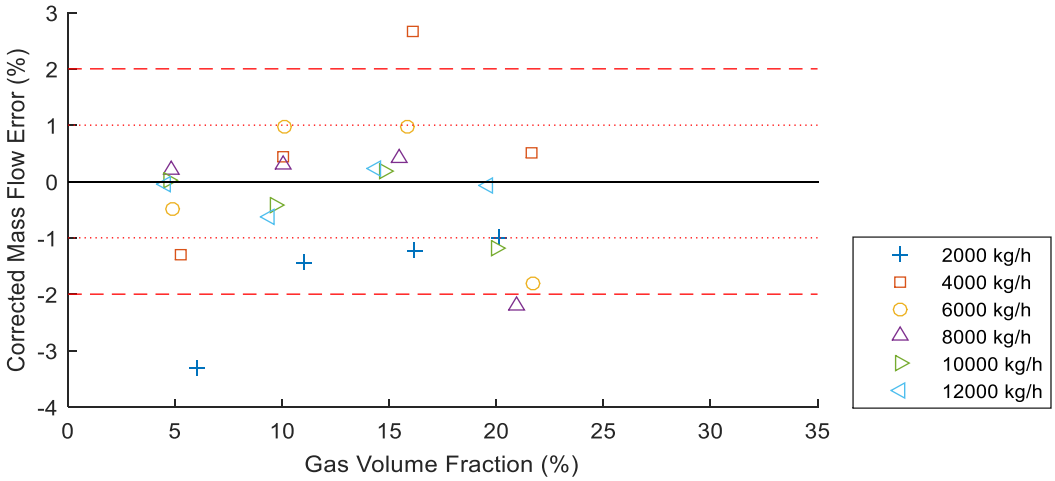

(d) Errors of the corrected mass flowrate on vertical pipeline with test dataset

Fig. 18. Errors of the corrected liquid mass flowrate error from the GPs.

As shown in Fig. 19, for the prediction of gas volume fraction, the outputs of GP models have large errors for low gas entrainment and low flowrates. The relative errors with test data reach 25% and -50% on horizontal and vertical pipes, respectively.

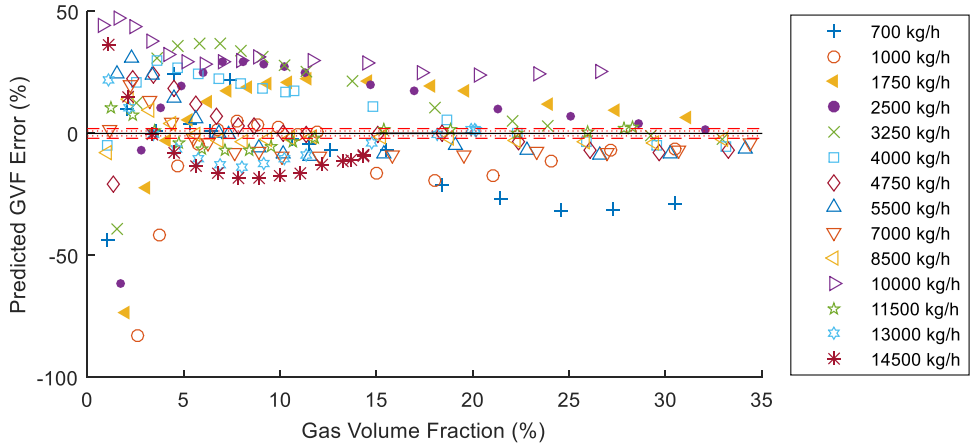

(a) Errors of the predicted gas volume fraction on horizontal pipeline with training dataset

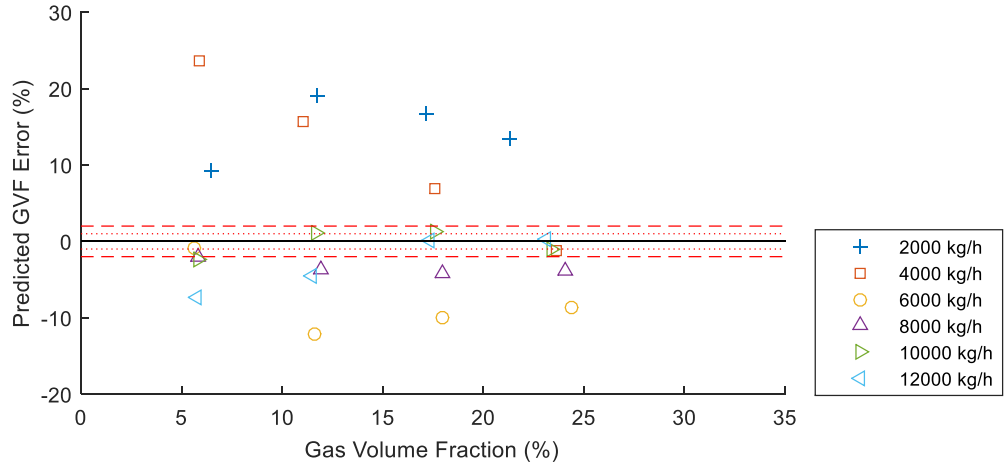

(b) Errors of the predicted gas volume fraction on horizontal pipeline with test dataset

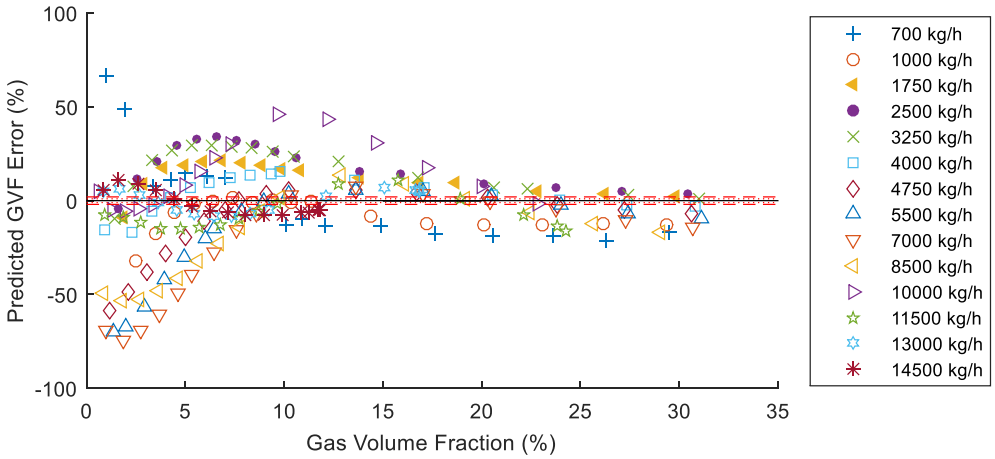

(c) Errors of the predicted gas volume fraction on vertical pipeline with training dataset

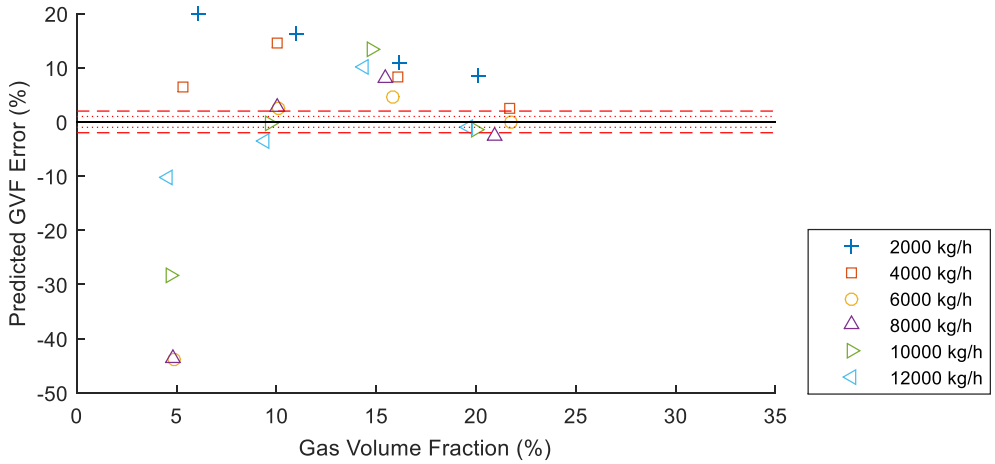

(d) Errors of the predicted gas volume fraction on vertical pipeline with test dataset

Fig. 19. Errors of the predicted gas volume fraction from the GPs.

H. Perforamce comparison between BP-ANN, RBF-ANN, SVM and GP

(1) Robustness

In order to assess the robustness of the four models for two-phase flow measurement, the averaged NRMSE values are shown in Fig. 20. The models for liquid mass flowrate correction and gas volume fraction prediction, GP produces larger errors than the other three techniques. Both BP-ANN and RBF-ANN have similar mean NRMSE with the training dataset, while the

SVM models yield less errors. With the test dataset, BP-ANN, RBF-ANN and SVM methods perform similarly on Model-H-L and Model-V-L. However the SVM models are significantly better than the BP-ANN, RBF-ANN and GP models for the prediction of gas volume fraction. Moreover, BP-ANN and RBF-ANN have uncertain parameters to optimize which could result in differences in performance. However, due to their fixed structure, the SVM models produce repeatable results all the time. This outcome suggests that the SVM models are superior to both ANN and GP models in term of robustness.

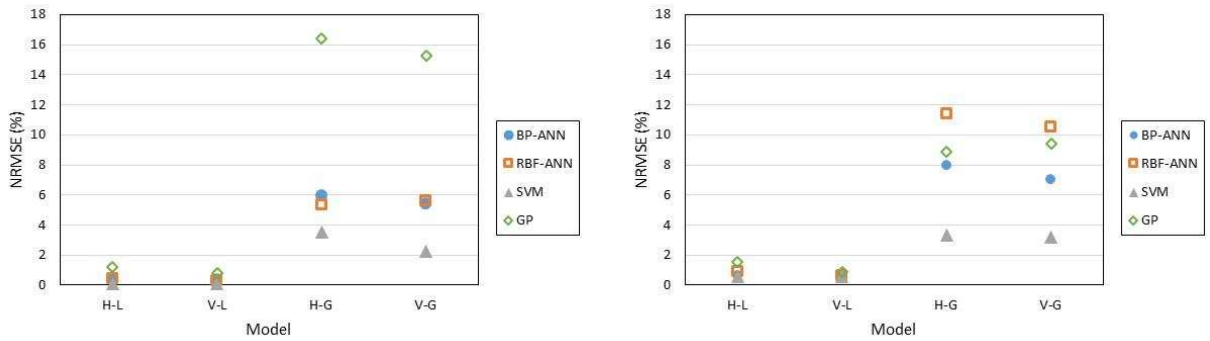

(a) ANNs, SVMs and GPs with training dataset (b) ANNs, SVMs and GPs with test dataset

Fig. 20. Performance comparison between ANNs, SVMs and GPs.

(2) Accuracy

Fig. 21 depicts the relative error histograms of the ANNs, SVMs and GPs for corrected liquid mass flowrate. It is clear that the error distributions of the GP and ANN models are much wider and dispersive than the SVM models. Through comparing the mean value and standard deviation of the errors between the eight error distributions (Table IV), we can see that the SVM models with the lowest mean value and standard deviation outperform the BP-ANN, RBF-ANN and GP models for liquid mass flowrate measurement on both horizontal and vertical pipelines. Moreover, the data driven models (mean value 0.0008% and standard deviation 0.40%) on the vertical

pipeline perform better than those on the horizontal pipeline (mean value 0.0585% and standard deviation 0.66%).

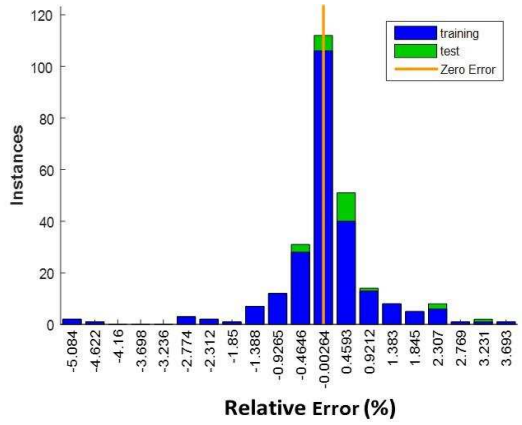

(1) BP-ANN: H-L

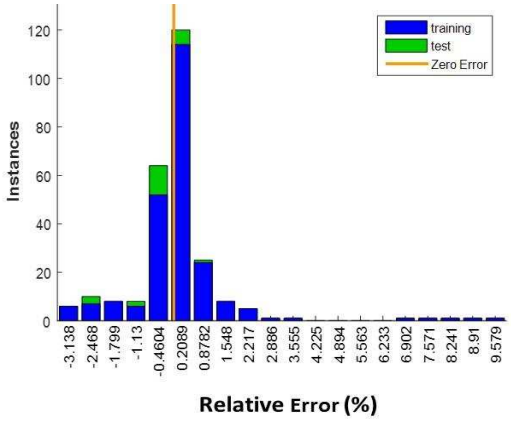

(2) BP-ANN: V-L

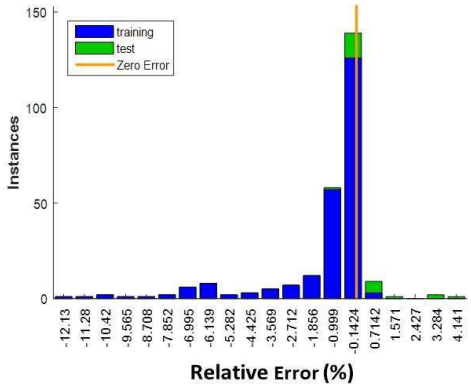

(3) RBF-ANN: H-L

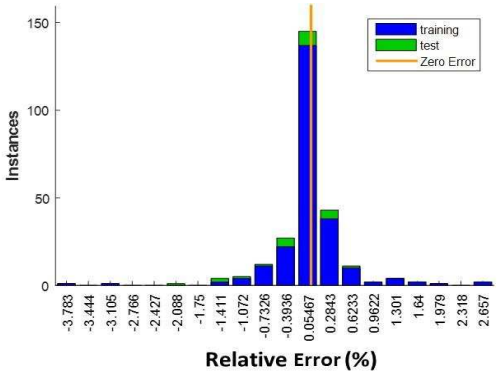

(4) RBF-ANN: V-L

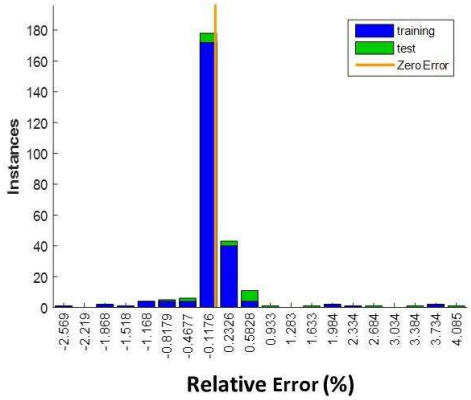

(5) SVM: H-L

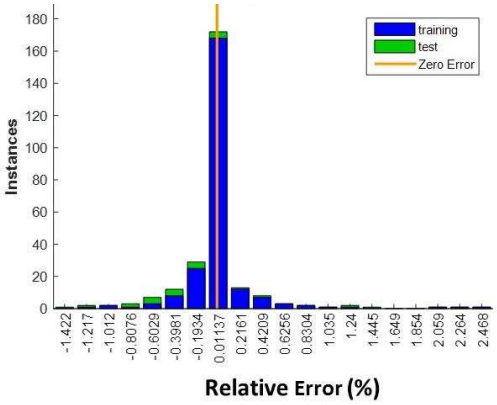

(6) SVM: V-L

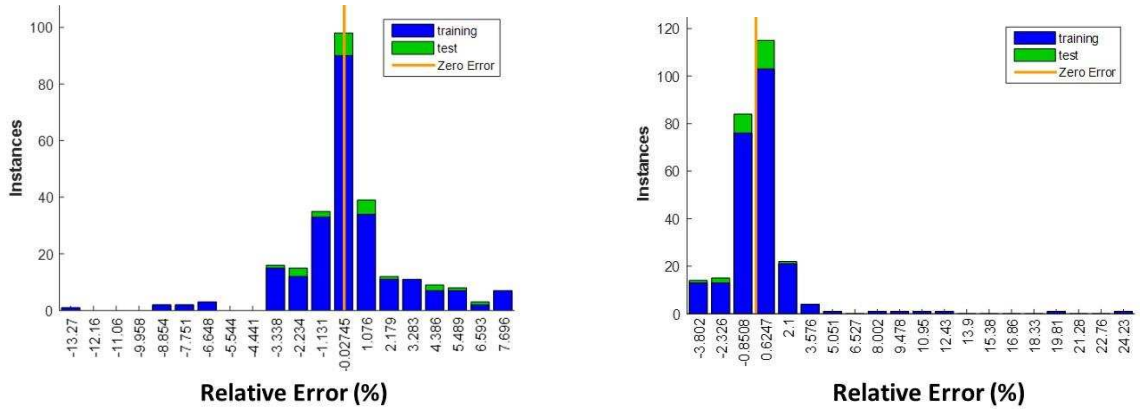

(7) GP: H-L (8) GP: V-L

Fig. 21. Relative error histogram of ANNs, SVMs and GPs for corrected liquid mass flowrate.

Table IV Mean and standard deviation of the relative error distribution for liquid mass flowrate correction

Model		BP-ANN	RBF-ANN	SVM	GP
Model H-L	Mean (%)	0.0823	1.2200	0.0585	0.2405
	Standard deviation (%)	1.03	2.30	0.66	2.83
Model V-L	Mean (%)	0.0548	-0.0248	0.0008	0.1660
	Standard deviation (%)	1.50	0.61	0.40	2.77

Fig. 22 shows the relative error histograms of the four kinds of models for gas volume fraction prediction. GP models have a larger range of errors than all other models. The error distribution of the SVM model is much narrower than the ANN models for the measurement of gas volume fraction. It can be seen that most errors of the SVM models are concentrated around zero line. Table V shows that the standard deviations of the SVM and RBF-ANN models are smaller than that of the BP-ANN and GP models on both horizontal and vertical pipelines.

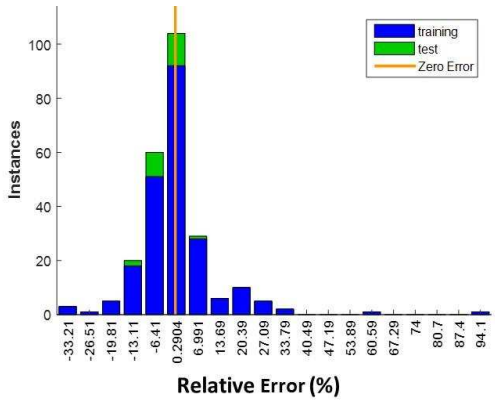

(1) BP-ANN: H-G

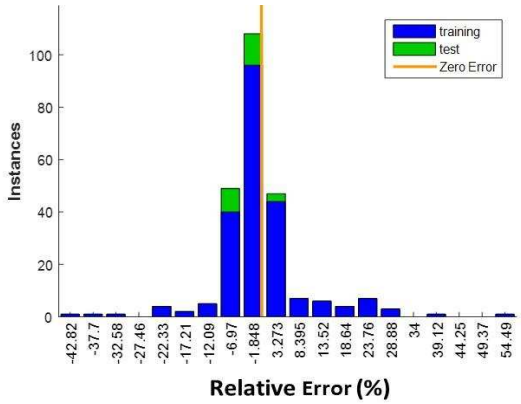

(2) BP-ANN: V-G

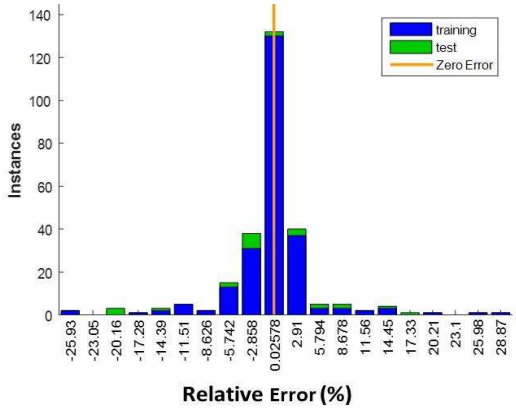

(3) RBF-ANN: H-G

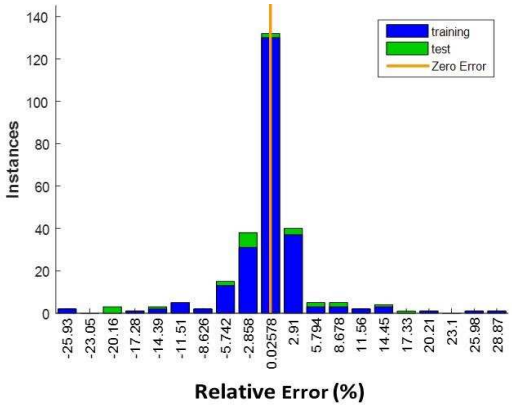

(4) RBF-ANN: V-G

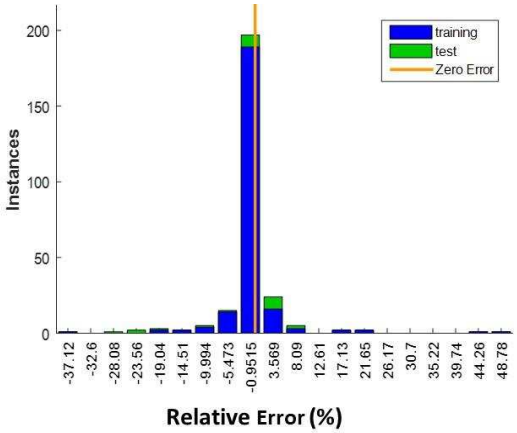

(5) SVM: H-G

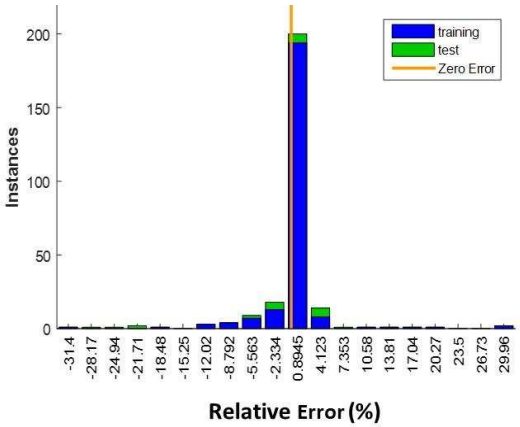

(6) SVM: V-G

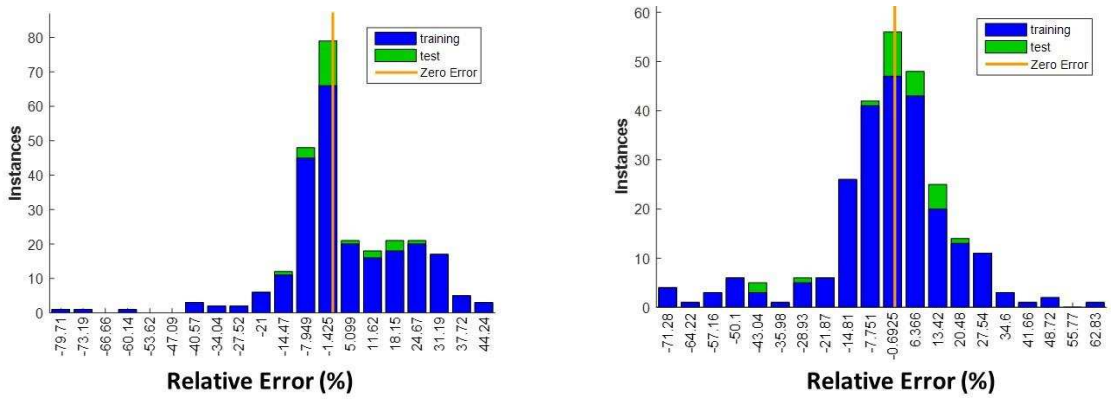

(7) GP: H-G (8) GP: V-G

Fig. 22. Relative error histogram of ANNs, SVMs and GPs for gas volume fraction prediction.

Table V Mean and standard deviation of the relative error distribution for gas volume fraction prediction

Model		BP-ANN	RBF-ANN	SVM	GP
Model H-G	Mean (%)	0.17	-0.26	-0.25	3.15
	Standard deviation (%)	11.88	6.02	6.95	17.70
Model V-G	Mean (%)	-0.18	0.50	-0.38	-1.99
	Standard deviation (%)	9.70	4.70	5.57	20.62

Table VI Accuracy comparisons of ANN, SVM and GP models

Model	H-L		V-L		H-G	V-G
Error limit	≤ ±2%	≤ ±1%	≤ ±2%	≤ ±1%	≤ ±10%	≤ ±10%
BP-ANN	91.95%	80.08%	89.66%	79.69%	79.31%	86.21%
RBF-ANN	82.76%	72.80%	97.70%	91.57%	90.80%	95.79%
SVM	96.93%	93.49%	98.85%	96.17%	93.10%	94.25%
GP	68.20%	54.41%	83.14%	67.05%	55.56%	54.79%

In order to assess the accuracy of the ANN, SVM and GP models, the percentage of experimental data for each model which can achieve the accuracy of ±2% and ±1%, respectively, for liquid mass flowrate measurement and ±10% for gas volume fraction prediction is calculated and summarized in Table VI. For liquid mass flowrate measurement with the SVM models, 93.49% of the experimental data yield a relative error less than ±1% on the horizontal pipeline whilst 96.17% of the results are within ±1% on the vertical installation. The SVM models predict the gas volume

fraction with a relative error less than 10% for 93.10% and 94.25% of the test conditions on horizontal and vertical installations, respectively. Therefore, the SVM models perform significantly better than the BP-ANN, RBF-ANN and GP models for two phase flow measurement in terms of robustness and accuracy.

IV. CONCULSIONS

In this paper, experimental and analytical investigations have been carried out to assess the performance of BP-ANN, RBF-ANN, SVM and GP for gas-liquid two-phase flow measurement using Coriolis flowmeters. Results presented have suggested that the SVM models are superior to the two ANN models and the GP models for two-phase flow measurement in terms of robustness and accuracy. The SVM models perform well consistently while the performance of ANN and GP models depends on the user-defined parameters. For liquid mass flowrate measurement, the SVM models outperform the BP-ANN, RBF-ANN and GP on both horizontal and vertical pipelines and the most corrected errors (>93%) are within ±1%. For the gas volume fraction prediction, the RBF-ANN and SVM models yield most relative errors (>90%) less than ±10% and outperform the BP-ANN and GP. It must be stressed that the significantly reduced errors in mass flowrate measurement from the Coriolis mass flowmeters and gas volume fraction prediction are achieved by using the existing data from the Coriolis flowmeters and a simple DP transducer without the use of any other devices. SVM has consistently outperformed ANN and GP in the correction of liquid mass flow errors and prediction of gas volume fraction. This outcome has effectively extended the applicability of Coriolis mass flowmeters to liquid flow measurement with a significant volume of entrained gas. In future work the data driven models will be extended for the measurement of other liquids with different viscosities under two-phase or multi-phase flow conditions.

ACKNOWLEDGMENT

The authors would like to acknowledge the financial support of the UK CCS Research Centre (www.ukccsrc.ac.uk) in carrying out this work. The UKCCSRC is funded by the EPSRC as part of the RCUK Energy Programme.

REFERENCES

[1] Y. Li, J. Wang and Y. Geng, "Study on wet gas online flow rate measurement based on dual slotted orifice plate," Flow Meas. Instrum., vol. 20, no. 4-5, pp. 168-173, Aug. 2009.

[2] J. Oliveira, J. Passos, R. Verschaeren and C. Geld, "Mass flow rate measurements in gas-liquid flows by means of a venturi or orifice plate coupled to a void fraction sensor," Exp. Therm. Fluid Sci., vol. 33, no. 2, pp. 253-260, Jan. 2009.

[3] Z. Sun, "Mass flow measurement of gas-liquid bubble flow with the combined use of a Venturi tube and a vortex flowmeter," Meas. Sci. Technol., vol. 21, no.5, pp. 1-7, 2010.

[4] Y. Xu, H. Wang, Z. Cui, F. Dong and Y. Yan, "Separation of gas-liquid two-phase flow through independent component analysis," IEEE Trans. Instrum. Meas., vol. 59, no. 5, pp. 1294-1302, May 2010.

[5] L. Wang, Z. Yao, B. Wang, H. Ji and H. Li, "Flow pattern identification of gas-liquid two-phase flow based on capacitively coupled contactless conductivity detection," IEEE Trans. Instrum. Meas., vol. 61, no. 5, pp. 1466-1475, May 2012.

[6] F. Dong, Y. Xu, L Hua and H. Wang, "Two methods for measurement of gas-liquid flows in vertical upward pipe using dual-plane ERT system," IEEE Trans. Instrum. Meas., vol. 55, no., 5, pp. 1576-1586, Oct. 2006.

[7] L. Xu, W. Zhou, X. Li and S. Tang, “Wet gas metering using a revised Venturi meter and soft-computing approximation techniques,” IEEE Trans. Instrum. Meas., vol. 60, no. 3, pp. 947-956, Mar. 2011.

[8] X. Li, X. Huang, B. Wang and H. Li, “A new method for the online voidage measurement of the gas-oil two-phase flow,” IEEE Trans. Instrum. Meas., vol. 58, no. 5, pp. 1571-1577, May 2009.

[9] H. Ji, J. Long, Y. Fu, Z. Huang, B. Wang and H. Li, “Flow pattern identification based on EMD and LS-SVM for gas-liquid two-phase flow in a minichannel,” IEEE Trans. Instrum. Meas., vol. 60, no. 5, pp. 1917-1924, May 2011.

[10] M. Giorgi, A. Ficarella and A. Lay-Ekuakille, “Cavitation regime detection by LS-SVM and ANN with wavelet decomposition based on pressure sensor signals,” IEEE Sens. J., vol. 15, no. 10, pp. 5701-5708, Oct. 2015.

[11] T. Wang and R. Baker, “Coriolis flowmeters: a review of developments over the past 20 years, and an assessment of the state of the art and likely future directions,” Flow Meas. Instrum., vol. 40, pp. 99-123, Sep. 2014.

[12] J. Hemp and G. Sultan, “On the theory and performance of Coriolis mass flowmeters,” in Proc. of the International Conference on Mass flow measurement Direct and Indirect, 1989.

[13] R. Liu, M. Fuent, M. Henry and M. Duta, “A neural network to correct mass flow errors caused by two-phase flow in a digital Coriolis mass flowmeter,” Flow Meas. Instrum., vol. 12, no. 1, pp. 53-63, Sep. 2001.

[14] B. Safarinejadian, M. Tajeddini and L. Mahmoodi, “A new fuzzy based method for error correction of Coriolis mass flow meter in presence of two-phase fluid,” in Proc. of International Conference on Artificial Intelligence and Image Processing, pp. 192-196, 2012.

[15] V. Lari and F. Shabaninia, “Error correction of a Coriolis mass flow meter in two-phase flow measurement using Neuro-Fuzzy, ” Proc. 16th CSI International Symposium on Artificial Intelligence and Signal Processing, pp. 611-616, Fars, Iran, 2-3 May 2012.

[16] Q. Hou, K. Xu, M. Fang, Y. Shi, B. Tao and R. Jiang, “Gas-liquid two-phase flow correction method for digital CMF,” IEEE Trans. Instrum. Meas., vol. 63, no. 10, pp. 2396-2404, Mar. 2014.

[17] L. Xing, Y. Geng, C. Hua, H. Zhu and A. Rieder, “A combination method for metering gas-liquid two-phase flows of low liquid loading applying ultrasonic and Coriolis flowmeters,” Flow Meas. Instrum., vol. 37, pp. 135-143, Jan. 2014.

[18] L. Ma, H. Zhang, H. Zhou, and Q. He, “Mass flow measurement of oil-water two-phase flow based on Coriolis flow meter and SVM,” Journal of Chemical Engineering of Chinese Universities, vol. 21, no. 2, pp. 201-205, Apr. 2007.

[19] R. May, H. Maier, G. Dandy and T. Fernando, Non-linear variable selection for artificial neural networks using partial mutual information, Environmental Modelling & Software, vol. 23, pp. 1312-1326, 2008.

[20] S. Galelli, G. Humphrey, H. Maier, A. Castelletti, G. Dandy and M. Gibbs, An evaluation framework for input variable selection algorithms for environmental data-driven models, Environmental Modelling & Software, vol. 62, pp. 33-51, 2014.

[21] L. Wang, J. Liu, Y. Yan, X. Wang and T. Wang, “Gas-liquid two-phase flow measurement using Coriolis flowmeters incorporating neural networks,” in Proc. IEEE Int. Instrum. Meas. Technol. Conf., pp. 747-751, Taipei, Taiwan, 23-26 May 2016.

[22] H. A. Farfani, F. Behnamfar and A Fathollahi, “Dynamic analysis of soil-structure interaction using the neural networks and the support vector machines,” Expert Syst. Appl., vol. 42, no. 22, pp. 8971-8981, Dec. 2015.

[23] S. Belaid and A. Mellit, “Prediction of daily and mean monthly global solar radiation using support vector machine in an arid climate,” Energ. Convers. Manage., vol. 118, pp. 105-118, June 2016.

[24] M. Ramli, S. Twaha and Y. Al-Turki, “Investigating the performance of support vector machine and artificial neural networks in predicting solar radiation on tilted surface: Saudi Arabia case study,” Energ. Convers. Manage., vol.105, pp. 442-452, Nov. 2015.

[25] F. Chen, H. Li, Z. Xu, S. Hou and D. Yang, “User-friendly optimization approach of fed-batch fermentation conditions for the production of iturin A using artificial neural networks and support vector machine,” Electron. J. Biotechnol., vol. 18, no. 4, pp. 273-280, July 2015.

[26] A. Gandomi and A. Alavi, “A new multi-genetic programming approach to nonlinear system modeling. Part I: materials and structural engineering problems,” Neural Comput. & Applic., vol. 21, no. 1, pp. 171-187, Feb. 2012.

[27] C. Cortes and V. Vapnik, “Support-vector networks,” Mach. Learn., vol. 20, pp. 273-297, 1995.

[28] H. Drucker, C. Burges, L. Kaufman, A. Smola and V. Vapnik, “Support vector regression machines,” Neural Inform. Process. Syst., vol.9, pp. 155-161, 1997.

[29] J. Koza, Genetic programming: On the programming of computers by means of natural evolution. MIT Press, Cambridege, 1992.

[30] J. Madar, J. Abonyi and F. Szeifert, “Genetic programming for the identification of nonlinear input-output models,” Ind. Eng. Chem. Res., vol. 44, no. 9, pp. 3178-3186, Mar. 2005.

[31] DP. Searson, GPTIPS 2: an open-source software platform for symbolic data mining, Chaper 22 in Handbook of Genetic Programming Applications, Springer, New York, NY, 2015.

[32] J. W. Kunze, R. Storm and T. Wang, “Coriolis mass flow measurement with entrained gas,” in Proc. of Sensors and Measuring Systems 2014, 17. ITG/GMA Symposium, Nürnberg, 2014.

[33] G. Bowden, H. Maier and G. Dandy, “Input determination for neural network models in water resources applications. Part 2. Case study: forecasting salinity in a river,” J. Hydrol., vol.301, no. 1-4, pp. 93-107, Jan. 2005.